



8-2011

## Positron Emission Tomography (PET) for Flow Measurement

Bi Yao Zhang  
bzhang5@utk.edu

Follow this and additional works at: [https://trace.tennessee.edu/utk\\_gradthes](https://trace.tennessee.edu/utk_gradthes)



Part of the [Bioimaging and Biomedical Optics Commons](#), [Fluid Dynamics Commons](#), and the [Nuclear Engineering Commons](#)

---

### Recommended Citation

Zhang, Bi Yao, "Positron Emission Tomography (PET) for Flow Measurement. " Master's Thesis, University of Tennessee, 2011.

[https://trace.tennessee.edu/utk\\_gradthes/1042](https://trace.tennessee.edu/utk_gradthes/1042)

This Thesis is brought to you for free and open access by the Graduate School at TRACE: Tennessee Research and Creative Exchange. It has been accepted for inclusion in Masters Theses by an authorized administrator of TRACE: Tennessee Research and Creative Exchange. For more information, please contact [trace@utk.edu](mailto:trace@utk.edu).

To the Graduate Council:

I am submitting herewith a thesis written by Bi Yao Zhang entitled "Positron Emission Tomography (PET) for Flow Measurement." I have examined the final electronic copy of this thesis for form and content and recommend that it be accepted in partial fulfillment of the requirements for the degree of Master of Science, with a major in Nuclear Engineering.

Arthurs E. Ruggles, Major Professor

We have read this thesis and recommend its acceptance:

Lawrence H. Heilbronn, Haitao Liao

Accepted for the Council:

Carolyn R. Hodges

Vice Provost and Dean of the Graduate School

(Original signatures are on file with official student records.)

# Positron Emission Tomography (PET) for Flow Measurement

A Thesis Presented for the  
Master of Science  
Degree  
The University of Tennessee, Knoxville

Bi Yao Zhang  
August 2011

Copyright © 2011 by Bi Yao Zhang  
All rights reserved.

### **Acknowledgements**

I would like to say thank you to everyone who has helped me with my college career. I would like to reserve a special appreciation for my major advisor, Dr. Arthur E Ruggles, for his dedication and patience in guiding me throughout my college education. I want to thank my committee members, Dr. Liao Haitao and Dr. Lawrence E Heilbronn, for taking time review my work. Special Thanks also to Dr. Jon Wall and Alan Stuckey of the UT Medical Center for providing access to the P4 PET scanner and for help with experiments and image processing. I also want to thanks all my friends and family for constant support throughout my education. Thank you all.

## Abstract

Positron Emission Tomography (PET) is frequently used for medical imaging. Maturity and flexibility of PET as an imaging technique has expanded its utility beyond the medical domain. It can be used as a tool for fluid flow studies in opaque fluids and for flow within complex geometry where conventional optical flow measurement approaches fail. This study explores the capabilities of PET as flow measurement tool suited to validation of computational fluid dynamic (CFD) predictions.

The MicroPET P4 scanner was used to image the diffusion process in flow around a rod bundle geometry similar to that found in a nuclear reactor fuel assembly. The PET data are compared with results from COMSOL CFD simulation and dye injection images. PET image resolution, acquisition speed and sensitivity are also examined in the context of flow measurement.

## Table of Contents

Chapter 1 Introduction and General Information.....	1
1.1 Introduction and Motivations.....	1
1.2 Objective.....	4
1.3 Report Organization.....	4
1.4 Original Contribution.....	4
Chapter 2 Positron Emission Tomography.....	6
2.1 History of Medical Imaging.....	6
2.2 Positron and Tracers.....	8
2.3 Radiation Shielding.....	11
2.3.1 Compton Scattering.....	12
2.3.2 Attenuation Coefficients.....	14
2.4 Ring Scanner: MicroPET P4.....	17
2.4.1 Scanner Design.....	19
2.4.2 Image Reconstruction of Algorithm.....	24
2.4.3 Filtered Backprojection.....	24
2.3.4 Iterative Reconstruction Algorithm.....	27
2.4.4 Expectation-Maximization (EM) Reconstruction.....	29
2.5 PET Spatial Resolution Physical Limits.....	30
2.6 Sensitivity.....	35
2.7 PET Data Correction.....	38
Chapter 3 Fundamental Fluid Dynamics.....	42
3.1 Flow Characteristic and Boundary Layer.....	42
3.2 Internal Flows.....	44
3.3 Fickian Diffusion.....	47
3.4 Advective Diffusion Process.....	48
3.5 Turbulence Advective Diffusion Equation.....	50
Chapter 4 Experiment using PET to Image Flow Mixing.....	54
4.1 Experiment Design.....	54
4.2 2X2 Test Section.....	57
4.3 2x2 Validation Cases: CFD and Dye test.....	60
4.4 Aluminum Rod Test Section.....	62
Chapter 5 Results and Discussion.....	65
Chapter 6 Conclusion and Future Work.....	81
List of References.....	83
Appendix A.....	86
Appendix B.....	89
Appendix C.....	90
Vita.....	92

## List of Tables

Table 2.1: Traditional PET Tracers .....	9
Table 2.2: MicroPET P4 System Specifications.....	18
Table 2.3: The Scintillator Crystal Properties.....	20
Table 2.4: The Positron Range in Various Materials.....	33
Table 2.5: The Linear Attenuation and Detection Efficiencies .....	38
Table 3.1: Square Array Hydraulic Area and Wetted Perimeter Evaluation .....	45
Table 3.2: Average Hydraulic Diameter Evaluation .....	46



## List of Figures

Figure 1.1:Boiling Water Reactor Core View .....	2
Figure 1.2: Computed Tomography (CT) for Reactor Core Studies .....	3
Figure 2.1: The First X-ray Image .....	6
Figure 2.2: The First Cyclotron .....	7
Figure 2.3: An Over View of PET Imaging.....	8
Figure 2.4: Positron Energy Spectrum.....	10
Figure 2.5: Annihilation Process.....	11
Figure 2.6: Photon Predominate Interaction as Function of Energy.....	12
Figure 2.7 Compton Scattering of Photon .....	13
Figure 2.8: The Mass Attenuation Coefficient .....	15
Figure 2.9: The Energy Absorption Coefficient .....	16
Figure 2.10: MicroPET P4 .....	18
Figure 2.11: Typical Photon Detector.....	19
Figure 2.12: The Common Block Detector.....	20
Figure 2.13: PMTs Coordinate System.....	21
Figure 2.14: PMT System Schematic .....	22
Figure 2.15: Coincidence Circuit.....	23
Figure 2.16: Type of Coincidence Counts .....	23
Figure 2.17: Projection Profile.....	24
Figure 2.18: Projection of Frequency Domain .....	25
Figure 2.19: The Ramp Filter.....	26
Figure 2.20: Overview of Iterative Image Reconstruction .....	27
Figure 2.21: The FWHM as Function of Distance .....	31
Figure 2.22: The Electron Range in Water .....	32
Figure 2.23: The Effective Positron Range.....	33
Figure 2.24: RMS Range for Positron in Water .....	34
Figure 2.25: Coincidence Counting with Multiple Crystals .....	36
Figure 2.26: The Parallel Beam Profile .....	37
Figure 3.1: Shear Force.....	42
Figure 3.2: Boundary Layer.....	43
Figure 3.3: Different Flow Regimes .....	47
Figure 3.4: The Control Volume.....	48
Figure 3.5: Turbulent Velocity Fluctuation .....	51
Figure 4.1: The 1 <sup>st</sup> Experiment Setup. ....	55
Figure 4.2: Closer View of Experiment Setup.....	55
Figure 4.3: Improved Experiment Design .....	57
Figure 4.4: A 2X2 Square Array Test Section.....	58
Figure 4.5: The 2X2 Test Section.....	58
Figure 4.6: Model in the COMSOL.....	60
Figure 4.7: Computational Meshes .....	61
Figure 4.8: Super Fine Mesh.....	61
Figure 4.9: 3 X 3 Square Array.....	63

Figure 4.10: The Aluminum Rod Test Section.....	63
Figure 4.11: Needle Location .....	64
Figure 5.1: 3-D Surface Contour of First Experiment Result from Amira.....	66
Figure 5.2: PET Result in AsiPro .....	67
Figure 5.3: Enhanced PET result in Amira.....	68
Figure 5.4: Result Comparison for PET and the Dye Test .....	69
Figure 5.5: Results Comparison for the COMSOL Model and the Dye Test.....	70
Figure 5.6: The Median Plane Comparison for Results form the PET and the COMSOL.....	71
Figure 5.7: Axial Slices for the PET Result at Specific Locations.....	72
Figure 5.8: Axial Slices for the COMSOL Result at Specific Locations .....	72
Figure 5.9: Axial Slices of the COMSOL and the PET Result Comparison .....	73
Figure 5.10: Different View of 1 <sup>st</sup> Test Result in IRW.....	74
Figure 5.11: A Closer View of the Result in IRW.....	75
Figure 5.12: Plume Volume versus Distance.....	76
Figure 5.13: The Activity as Function of Time .....	76
Figure 5.14: Activity as Function of Distance .....	77
Figure 5.15: 2nd Experiment Result .....	78
Figure 5.16: Slice View of the Plume.....	78
Figure 5.17: Different Views of Experiment 3 Result.....	79

## Chapter 1

### Introduction and General Information

#### 1.1 Introduction and Motivations

Within the fluid engineering community, Computational Fluid Dynamic (CFD) codes, such as COMSOL, RELAP 5, Star CD, FLUENT and others are commonly used for flow simulations. The uncertainty within the CFD code is often undocumented and difficult to quantify even for a specific type of flow simulation. Recent forming of CFD verification and validation standards, such as the ASME V&V 20 [25], are beginning to address need for quantified uncertainty in CFD outcomes. Particle Image Velocimetry (PIV) and Laser Doppler Velocimetry (LDV) are currently the two main methods used to study fluid flow. These methods are not well suit for study of some engineering systems, such as a nuclear reactor core, with complex geometry and opaque flow boundaries. An example nuclear core and its sub components are shown in figure 1.

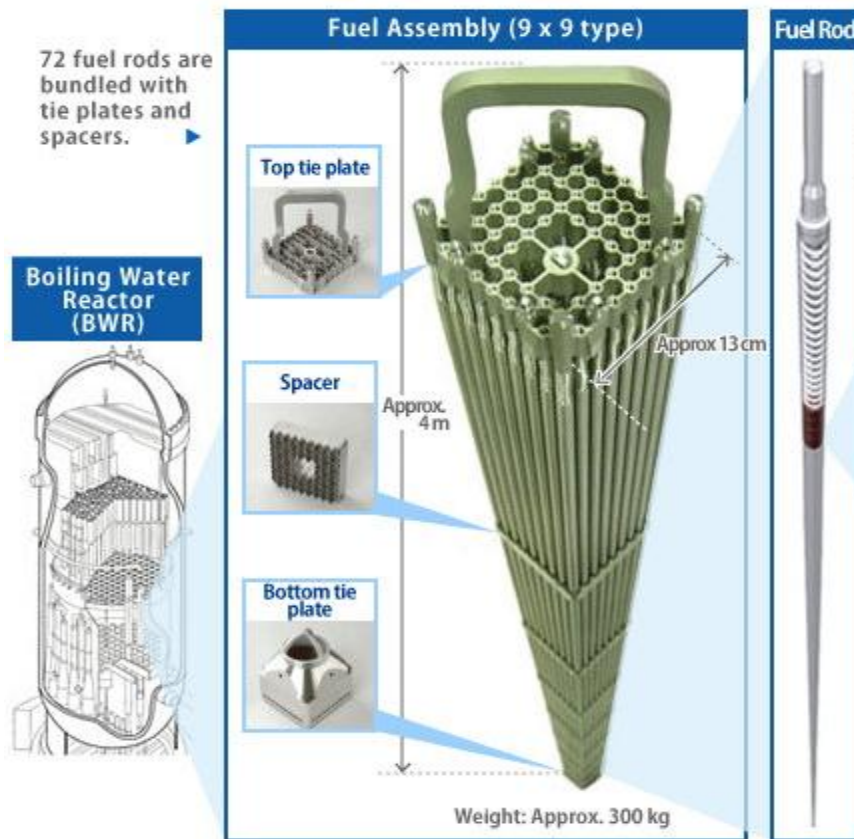


*Figure 1.1: Boiling Water Reactor Core View [14]*

Understanding of fluid behaviors within the reactor core is critical for reactor system efficiency and safety. Computed Tomography (CT), another common medical imaging technique, was used by Mitsubishi Heavy Industry, in Japan, in the early 90s to study thermal fluid behavior within the reactor core [3]. The experiment setup is shown in figure 1.2.

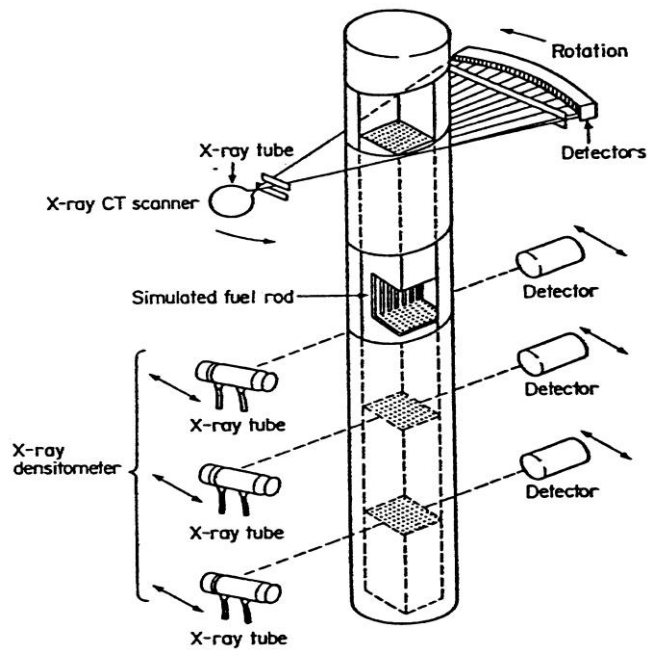


Figure 1.2: Computed Tomography (CT) for Reactor Core Studies [3]

CT is a common medical procedure for cancer and tumor detection. It uses an x-ray source that is rotated around the subject to map density variation of tissue within the patient. As for reactor core studies, the density variation of coolant was mapped in a fuel assembly. The accuracy of this method is very well established using phantoms with  $\pm 2\%$  liquid density and  $\pm 0.2$  mm spatial resolution reported. Results of CT were compared with CFD predictions by Tentner and Pointer in 2009. Other nuclear imaging approaches, such as Positron Emission Tomography (PET), could be used for flow measurement. PET method uses a tracer, a positron emitting atom inside a larger molecule, which selectively interacts with tumor cells. Fluorine 18 attached to glucose, fludeoxyglucose (FDG) is the most commonly used tracer for medical PET applications. The locations where the glucose is metabolized are “imaged” as regions of higher activity. The image is a field of activity per unit volume values usually reported in  $\mu\text{Ci}$  per  $\mu\text{L}$ .

Maps of activity in a mixing flow of FDG and water could be used to validate CFD prediction of flow mixing and forms the basis for the studies presented here.

## **1.2 Objective**

This research explores the basic capability of PET for flow mixing and turbulent diffusivity studies. Experiments are designed to study and analyze the performance of PET for fluid flow study around a four rod bundle typical of a nuclear fuel sub-channel. The objective is to examine suitability of PET as a tool for fundamental fluid studies. Results from these experiments are used to determine the capability of PET as a validation tool for CFD simulation codes. The ultimate goal is to expand PET into thermal fluid studies of nuclear reactor components and other complex flow geometries.

## **1.3 Report Organization**

Chapter 2 covers the history, background and theory behind PET. The fundamental fluid dynamics covered in chapter 3 includes laminar and turbulent flows and diffusion theory. Chapter 4 covers the experimentation and case studies. It covers experimental design setup and challenges encountered. A COMSOL CFD simulation and the dye test are also included in Chapter 4. Results and discussions are presents in Chapter 5, which includes comparisons between dye traces, CFD outcomes and PET image derived data. Types of results and methodology of data analysis are also discussed in Chapter 5. The final chapter covers conclusions and future work.

## **1.4 Original Contribution**

PET is well developed for medical applications and is now often used in plant sciences research. The only prior use of PET for study of engineering flows in found in

the UK at the University of Birmingham, where Dr. David Parker and others have developed a method for tracking particles in chemical reactors and separation equipment [24]. The use of PET to image advection diffusion flow phenomena, as developed herein, is entirely new.

## Chapter 2

### Positron Emission Tomography

Positron Emission Tomography (PET) and thermal fluid science are presently two completely different domains of science. In order to incorporate PET into thermal fluid studies, a comprehensive understanding of both PET and flow behavior is required. The historical overview of medical imaging, theories behind PET, scanner design and spatial resolution and sensitivity performance of PET are reviewed. General radiation detection and shielding methods also discussed in this chapter.

#### 2.1 History of Medical Imaging

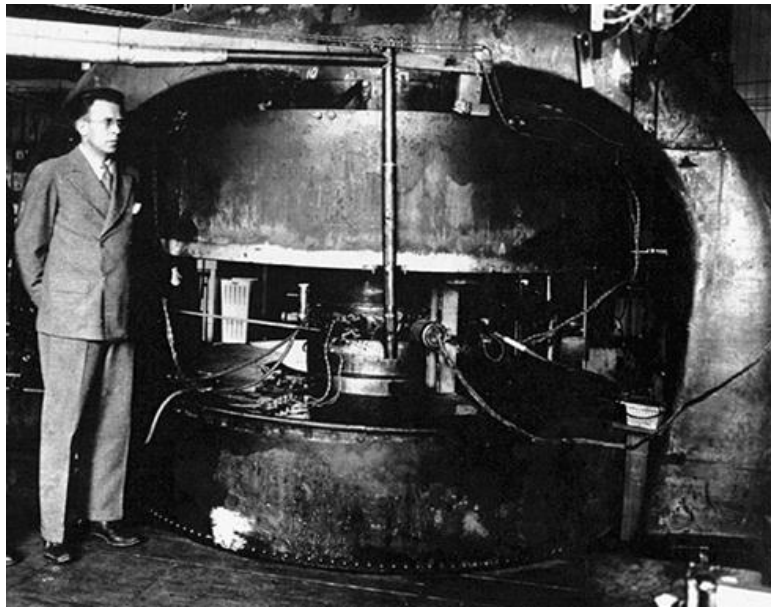
History of medical imaging traces back to the discovery of the x-ray by Wilhelm Roentgen in 1895 [12]. The famous first x-ray image [15] was produced by Wilhelm using his wife's hand in the same year, shown in figure 2.1.



Figure 2.1: The First X-ray Image [15]



Radioactivity is discovered by Henri Becquerel in the year of 1896. Two years later, radium is found by Marie Curie [12]. A major breakthrough happened in the year of 1913: Georg de Hevesy introduced principles of the radiotracer [6]. In 1923, the tracer concept was tested with plants in studies of biological process in absorptions and translocation of radioactive lead nitrate [7]. In 1927, the first human study with a radioactive tracer was done by Blumgart and Weisis [4]. They studied the transit time of blood from one arm to the other using radon. The invention of the cyclotron by Ernest O. Lawrence in 1930 set a major milestone for nuclear imaging [10]. It allowed for the production of artificial radionuclides and made a wide variety of biological process studies possible. The first cyclotron is shown in figure 2.2.



*Figure 2.2: The First Cyclotron [13]*

Radioactive isotopes from nuclear facilities became available for medical applications after World War II. Major mile stones for nuclear imaging were set in the 1950s. These include the invention of the Anger camera and the concept of the positron emitter. The Anger camera was invented by Hal Anger [1], and it was the first single-photon imaging system. A new page was opened in modern nuclear medicine imaging in the 1970s. The development of mathematical models for tomography reconstruction made three dimensional (3-D) presentations available [5]. Nuclear medicine imaging is divided into two major classes: single photon emission computed tomography (SPECT) and positron emission tomography (PET). PET and SPECT imaging modalities are similar; PET uses a positron emitter as tracer, with the positron annihilating to produce two coincident photons used for imaging. SPECT uses tracers that produce a single photon used for image construction.

## 2.2 Positron and Tracers

An overview of the PET imaging process is shown in figure 2.3.

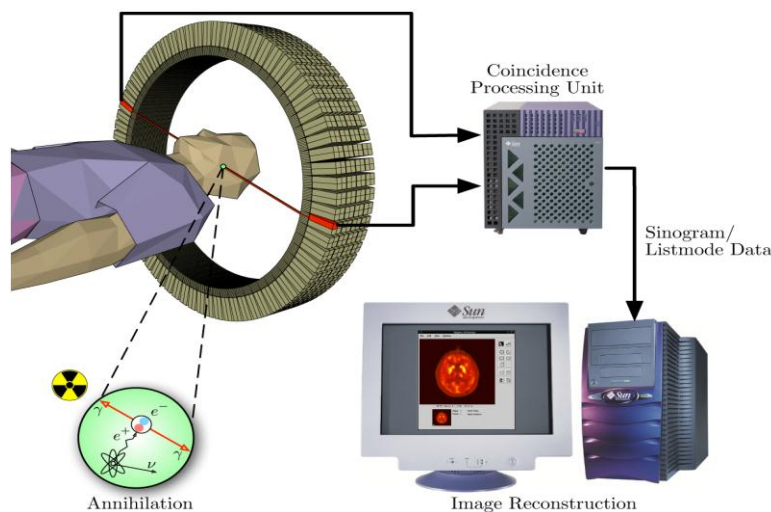


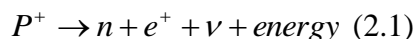
Figure 2.3: An Over View of PET Imaging [9]

The imaging process begins with injecting a type of radioactive tracer into a patient. PET uses different radiopharmaceutical tracers for various types of studies. A list of traditional PET tracers, their half-lives and maximum positron energies are shown in table 2.1. F-18 in the form of fludeoxyglucose (FDG) is the most frequently used tracer in clinical and research communities.

*Table 2.1: Traditional PET Tracers (Values are obtain from reference 26)*

<b>Nuclide</b>	<b>Half Life (minute)</b>	<b>Max Positron Energy(MeV)</b>
C-11	20.11	.96
F-18	110	.6335
O-15	2	1.732
N-13	10	1.198

The tracer will decay through a process called positron emission,  $\beta^+$  decay. The decay process is described by equation 2.1. A proton “P” is converted into a neutron “n” and positron “ $e^+$ ” plus neutrino “ $\nu$ .” A positron is just a positively charged electron. For the  $\beta^+$  process to occur, the mass difference between the parent atom and daughter must be greater than two rest mass of electron, corresponding to energy equal to  $2mC^2$ , which is equivalent to 1.022 MeV. This process is exothermic, with external energy release Q. The external energy release is equal to the maximum kinetic energy of the positron immediately following decay. The total energy release can be estimated with equation 2.2.



$$Q \cong M(A, Z)c^2 - M(A, Z-1)c^2 - 2mC^2 \quad (2.2)$$

An energy spectrum of a positron is shown in figure 2.4. The  $E_{\text{max}}$  represents the maximum kinetic energy a positron particle has during a reaction. The average kinetic energy for a positron can be estimated as 1/3 of the maximum energy [20].

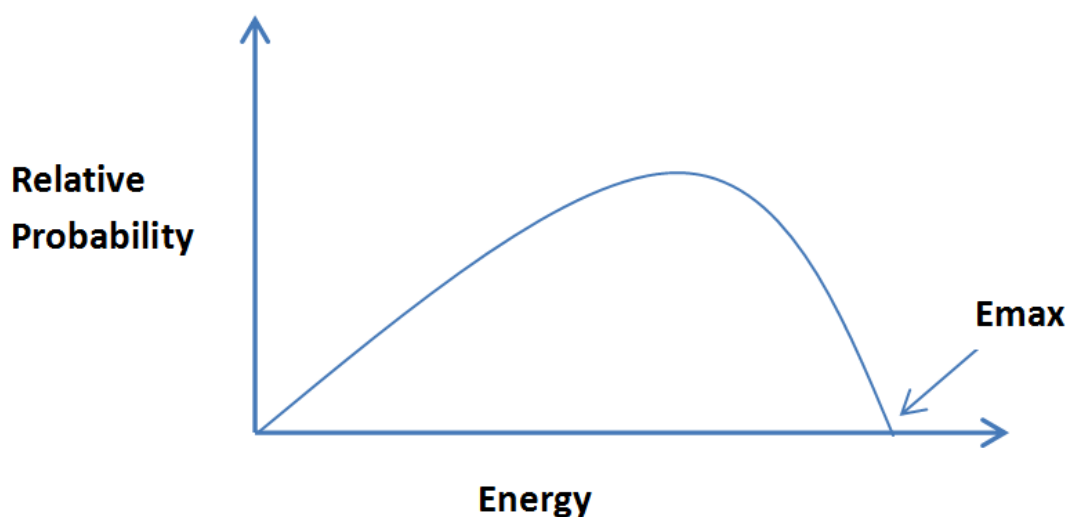


*Figure 2.4: Positron Energy Spectrum*

A positron is ejected from a nucleus with a certain kinetic energy that will be lost through interactions with surrounding matter. As the positron comes to rest, it will bind with a free electron to form an atom called “positronium”. A positronium has an extremely short half-life, equivalent to  $10^{-10}$  sec [5]. It decays through an annihilation reaction, which is shown in figure 2.5. After the annihilation reaction, two 0.511 MeV gamma rays are released simultaneously in opposite directions, very nearly 180 degrees apart. These two gamma rays are also known as coincidence gammas. These coincidence gammas are detected by the coincidence detector.

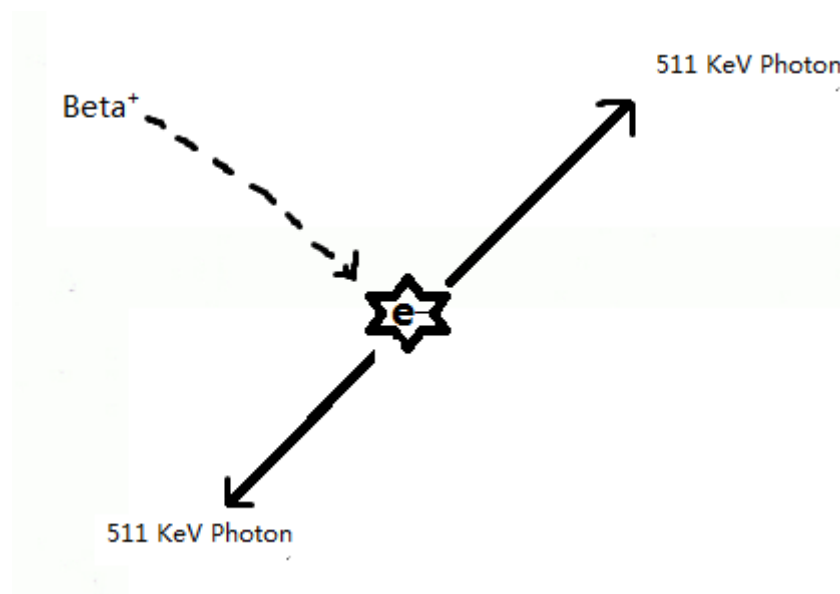


*Figure 2.5: Annihilation Process*

### 2.3 Radiation Shielding

As discussed in the previous sections, the main radiation concerns with PET are positrons and photons. Since the maximum range of a positron in water is about 1 mm, it is unlikely to be the main radiation threat. In comparison, annihilation photons have 511keV, which is a much greater radiation hazard. This is the main source of radiation exposure for both the patient and doctor during regular PET. The distance of photon travel in matter depends on the statistical probability of interaction per unit distance travel, also known as the attenuation coefficient. For photon shielding, it is important to understand the fundamental photon interaction mechanisms and attenuation coefficients.

### 2.3.1 Compton Scattering

There are four main energy loss mechanisms for photons: photoelectric absorption, Compton scattering, pair production and photonuclear reaction. The predominating interaction for a photon as a function of energy and atomic number is shown in figure 2.6.

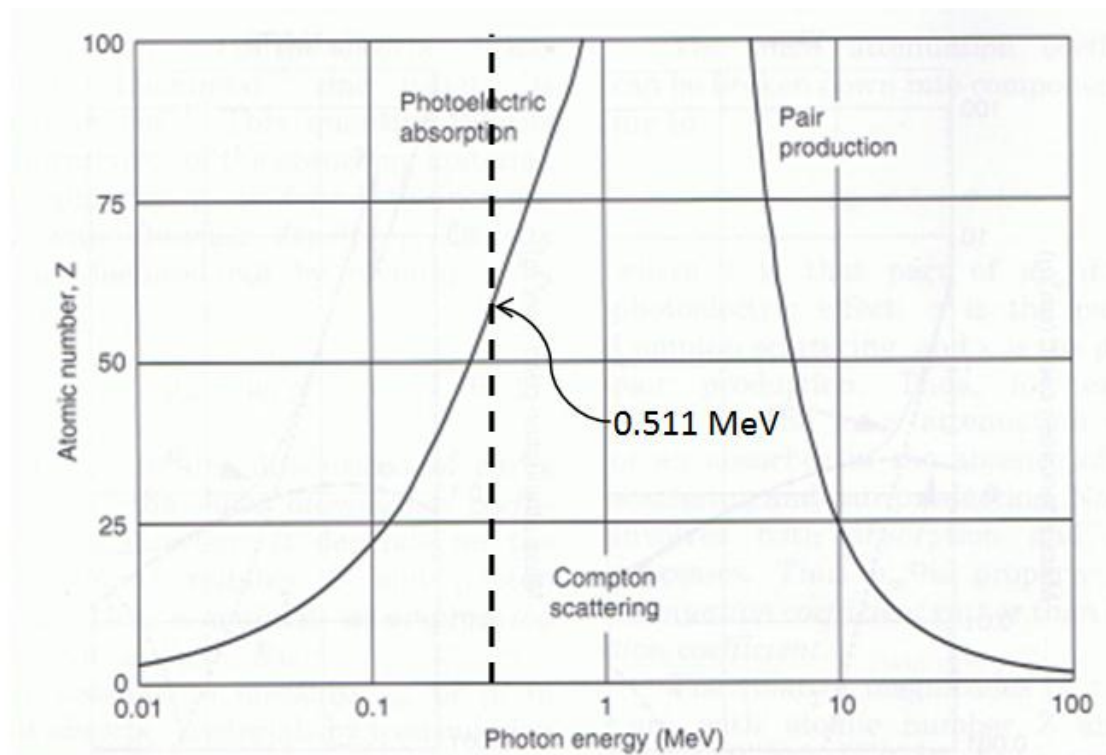
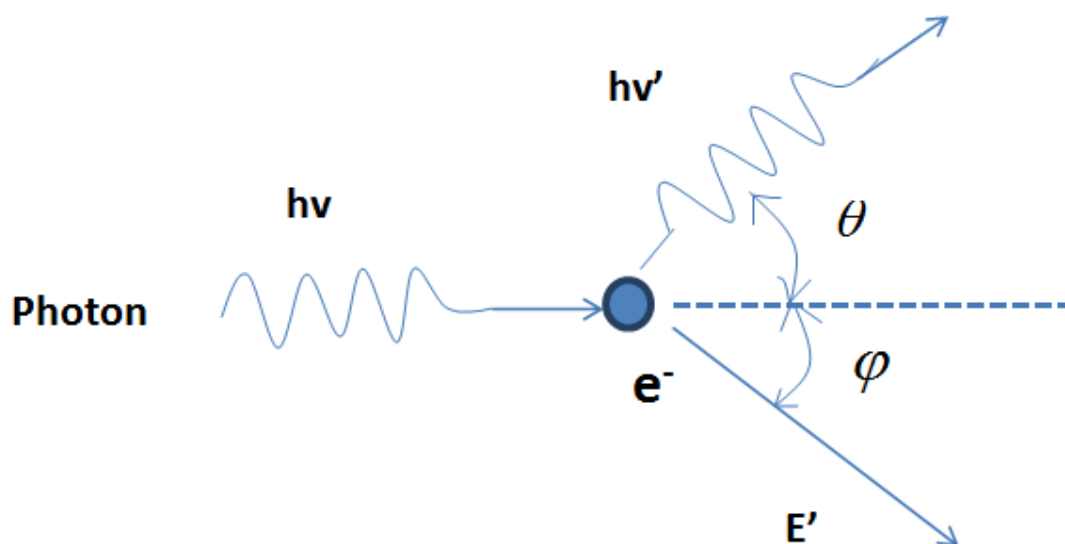


Figure 2.6: Photon Predominate Interaction as Function of Energy [5]

The Thomson and Rayleigh (coherent) scattering are also possible photon interactions, but there is nearly no energy transferred during these processes [21]. Photoelectric absorption is more probable for lower energy photons. Pair production is only possible when photon energy is greater than 1.022 MeV. The photo nuclear reaction generally occurs when photons have energy greater than several MeVs. For 511 KeV photons, the most probable interaction is Compton scattering. The Compton scattering interaction is

shown in figure 2.7. An incident photon with kinetic energy,  $h\nu$ , collides with a stationary free electron. The rest mass of electron corresponds to energy equal to  $mC^2$ , which is approximately 0.511 MeV. Only part of the photon energy is transferred to the electron during the collision process. The photon has remaining energy,  $h\nu'$ , after the collision, traveling in an altered trajectory. The electron recoils at a certain angle with kinetic energy  $E'$ .



*Figure 2.7 Compton Scattering of Photon*

The total energy is conserved for the Compton scattering event which is described in equation 2.3.

$$h\nu + mC^2 = h\nu' + E' \quad (2.3)$$

Momentum in Compton scattering is also conserved, and the conservation of momentum in the x and y directions is shown in equations 2.4 and 2.5. The initial momentum of the

photon is  $\frac{h\nu}{c}$ , and the final photon momentum is  $\frac{h\nu'}{c}$ . The final electron momentum is  $P'$ .

$$X : \frac{h\nu}{c} = \frac{h\nu'}{c} \cos \theta + P' \cos \varphi \quad (2.4)$$

$$Y : \frac{h\nu}{c} \sin \theta = P' \sin \varphi \quad (2.5)$$

The final photon energy after a collision can be calculated with equation 2.6.

$$h\nu' = \frac{h\nu}{1 + (h\nu/mc^2)(1 - \cos \theta)} \quad (2.6)$$

The final energy of a Compton electron is the difference between initial and final photon energy. The relationship between the scattered photon and the recoiled electron is described by equation 2.7.

$$\cot \frac{\theta}{2} = \left(1 + \frac{h\nu}{mc^2}\right) \tan \varphi \quad (2.7)$$

### 2.3.2 Attenuation Coefficients

The mass attenuation coefficient is essential knowledge for radiation shielding. As mentioned in the past, the attenuation coefficient is defined as the statistical probability of interaction per unit distance. It is denoted by  $\mu$ , and is greatly dependant on photon energy and the type of medium traversed. Its unit is inverse length, such as  $\text{cm}^{-1}$ . The mass attenuation coefficient,  $\mu/\rho$ , is defined as the linear attenuation divided by the density of material. It represents the probability of an interaction in the material traversed. The mass attenuation coefficient is more frequently used because it is independent of the physical phase of the material. Transmission is defined as the



probability of a photon penetrating a certain material without interaction, as shown in equation 2.8.

$$N(x) = N_0 e^{-\mu/\rho \cdot \rho \cdot x} \quad (2.8)$$

The mass attenuation coefficient as a function of energy for various materials is shown in figure 8.

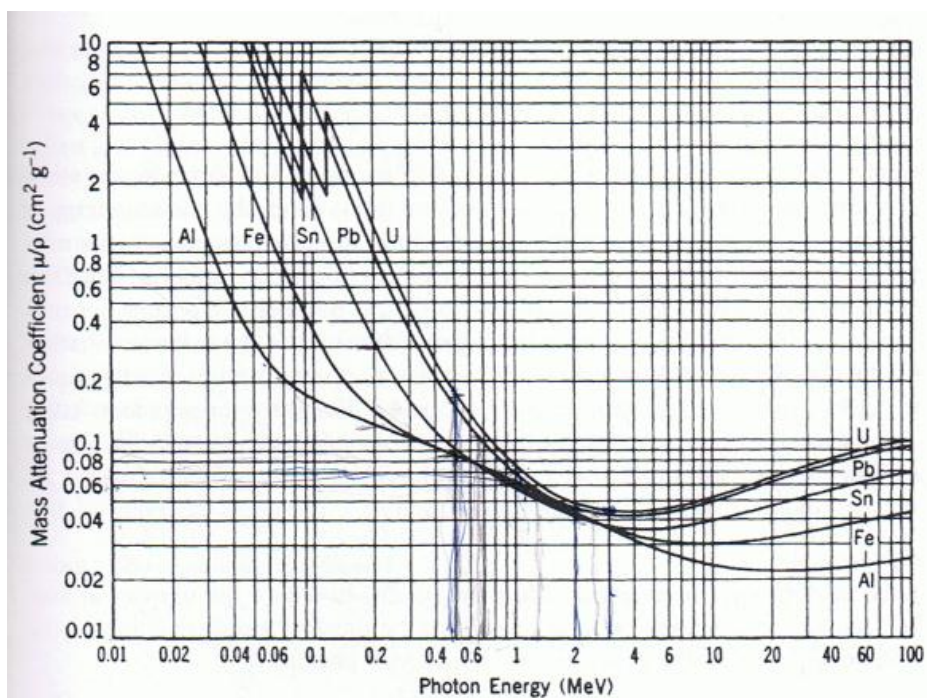


Figure 2.8: The Mass Attenuation Coefficient [13]

For a photon, more dense or high Z materials have greater attenuation and absorption. The attenuation decreases rapidly with increases in photon energy. The thickness of the absorbing material is inversely proportional to transmission. The obvious deduction that an increase in the absorbing material thickness reduces transmission, and vice-versa, is also true. Lead is a great choice of photon shielding material since it has excellent

attenuation and is very economical. For a 511 KeV photon, 99% of photon can be shielded with 2.54 cm of lead.

For dosimetry, energy absorption and energy transfer are subjects of interest. Energy absorption or energy transfer can be estimated with equation 2.9.

$$E' = Ee^{\mu_{en}T} \quad (2.9)$$

$\mu$  in the equation can be substituted for by the energy absorption coefficient  $\mu_{en}$  for energy absorption calculation. The mass energy absorption coefficient for various materials can be found in figure 2.9.

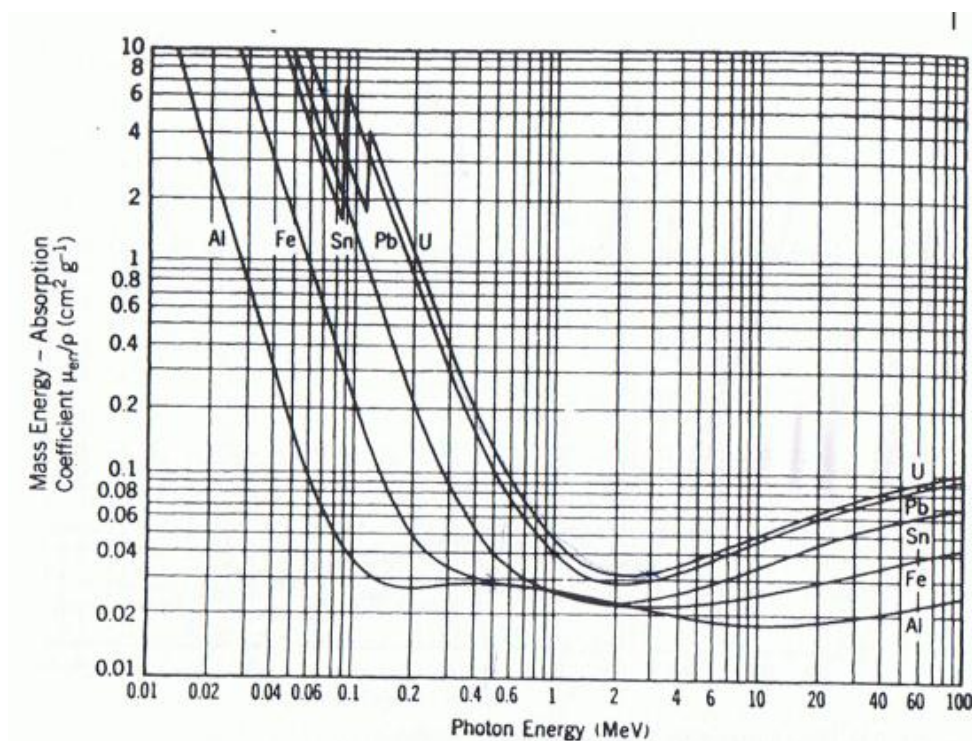


Figure 2.9: The Energy Absorption Coefficient [13]

The energy transfer coefficient  $\mu_{tr}$  is related to the energy transfer coefficient  $\mu_{en}$ , which is shown in equation 2.10.

$$\mu_{en}/\rho = \mu_{tr}/\rho (1-g) \quad (2.10)$$

$g$  in equation 2.10 represents the average fraction of the initial kinetic energy that is converted to bremsstrahlung. The average dose rate  $\dot{D}$  can be estimated with equation 2.11.

$$\dot{D} = \dot{\psi}^* \frac{\mu_{en}}{\rho} \quad (2.11)$$

#### 2.4 Ring Scanner: MicroPET P4

PET scanner designs are commercially available in rotational and stationary ring shapes. Rotational and stationary ring shape scanners are not very different; the major difference is in the respective shapes. Rotational scanners have at least one parallel set of detectors mounted to the gantry head that rotates around the patient to obtain an image, while the stationary ring scanners have detectors arranged in a ring shape. The number of detectors varies with the size of the ring. The stationary ring scanner is the main focus for this report since this type of scanner was used for this study. All stationary ring scanners have similar design, with the main differences lying in the size and type of scintillation crystal. MicroPET P4 is the PET scanner that was used for this study. It is a preclinical scanner mainly used for small animal studies designed to have very high spatial resolution. A photo of MicroPET P4 is shown in the figure 2.10.



*Figure 2.10: MicroPET P4 [11]*

The MicroPET P4 system specifications are available in table 2.2.

*Table 2.2: MicroPET P4 System Specifications[19]*

MicroPET	P4
Animal Port Diameters	22 cm
Axial Field of View	8 cm
Timing Window	2, 6, 10, 14, or 18 nsec
Energy Window	Variable: 0 – 810 KeV
Absolute System Sensitivity	2.25%
Reconstructed Spatial Resolution	~ 1.8 mm
Reconstructed Volumetric Resolution	~ 6.4 $\mu$ L

### 2.4.1 Scanner Design

A stationary ring scanner is formed by multiple detector assemblies. Each detector assembly, as shown in figure 2.11, has a block of scintillation crystal that is coupled to a photon detector. During the imaging process, as an annihilation photon enters the scintillator, the photon deposits some or all of its energy into the crystal, which produces light of a wavelength within the visible spectrum.

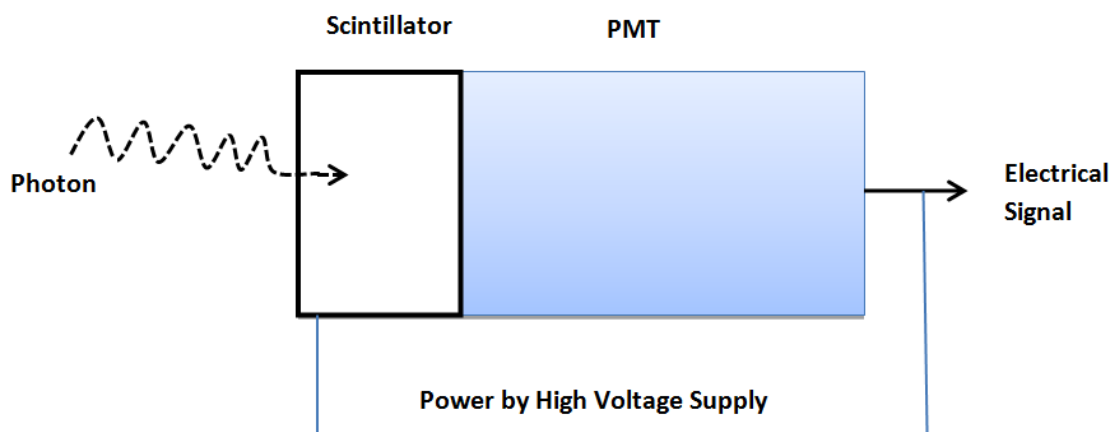


*Figure 2.11: Typical Photon Detector*

Sodium-Iodine (NaI) is a typical choice of scintillation crystal for photon detection since it is not expensive and performs reasonably well. However, NaI is relatively inefficient for higher energy photon detection, such as annihilation photons. The attenuation coefficient in the detector is proportional to the density of material and is defined as the photon's probability of interaction per unit distance traveled in the material. Bismuth Germanate (BGO) crystal and Lutetium Oxyorthosilicate (LSO) crystal are denser and have much faster decay time compared to NaI and are now the preferred detector crystals in PET scanners. A list of crystals and material properties are shown in table 2.3.

Table 2.3: The Scintillator Crystal Properties [2]

Scintillator	Density (g/cc)	Light output (photons per 511 keV)	Decay time (ns)	Index of refraction	Linear attenuation at 511 keV ( $\text{cm}^{-1}$ )	Ratio between photoelectric and Compton
Sodium iodide [NaI(Tl)]	3.67	19400	230	1.85	0.34	0.22
Bismuth Germanate (BGO)	7.13	4200	300	2.15	0.96	0.78
Lutetium Oxyorthosilicate (LSO:Ce)	7.40	~13000	~47	1.82	0.88	0.52
Gadolinium Oxyorthosilicate (GSO:Ce)	6.71	~4600	~56	1.85	0.70	0.35
Barium Fluoride (BaF <sub>2</sub> )	4.89	700, 4900	0.6, 630	1.56	0.45	0.24
Yttrium Aluminum Perovskite (YAP:Ce)	5.37	~9200	~27	1.95	0.46	0.05

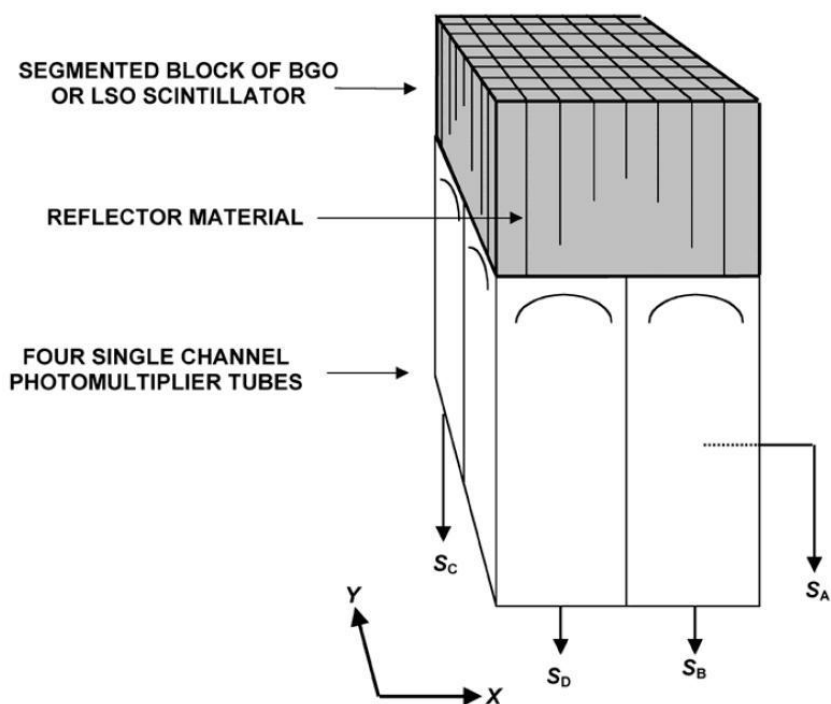
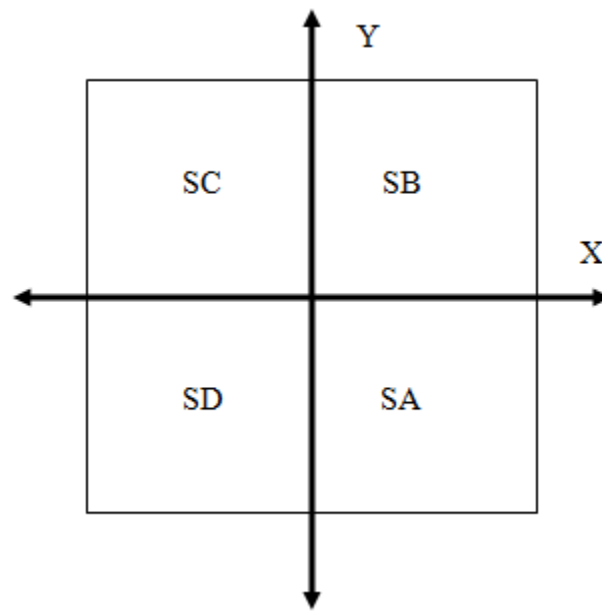


Figure 2.12: The Common Block Detector [5]

The block of scintillator is usually partially cut into segments, as shown in figure 2.12, producing an array of crystals, using a very fine saw. The voids created by the saw

between crystal regions are filled with reflector materials to reduce and control optical cross walk. The depth of saw cut is controlled so some intensity of light is delivered to all four photo multiplier tubes (PMT). An example of block detector design is shown in figure 2.12. The position of photon generation in the detector block is determined from the signal from the four-PMT array. Using the coordinate system presented in figure 2.13, the X and Y position of the positron can be determined using equation 2.12 and 2.13.



*Figure 2.13: PMTs Coordinate System*

$$X = (SA + SB - SC - SD) / (SA + SB + SC + SD) \quad (2.12)$$

$$Y = (SB + SC - SA - SD) / (SA + SB + SC + SD) \quad (2.13)$$

The PMT converts the light signal to an electrical signal. The conversion process is shown in figure 2.14. The light photon strikes the entrance window that is coated with a photoemissive substance which ejects a photoelectron. Cesium antimony (CsSb), a bialkali compound, is a common photoemissive substance. The conversion efficiency of



light photon to photoelectron is known as the quantum efficiency. Quantum efficiency is a function of wavelength with a peak at 400 nm of 25% [5]. The photoelectron is directed by the focusing grid toward the dynode. The dynode has positive charge often maintained near 200-400 volts [5]. The dynode is also coated with emissive material. As the photoelectron strikes the dynode, secondary electron is ejected from the dynode. The multiplication factor depends on the voltage difference between the dynode and cathode. A typical value for multiplication factor is 3 to 6 per dynode. Secondary electrons are attracted by the next dynode that is maintained at 50-150 volts higher potential [5]. Multiplication repeats for additional dynodes, and showers of electrons are collected at the anode.

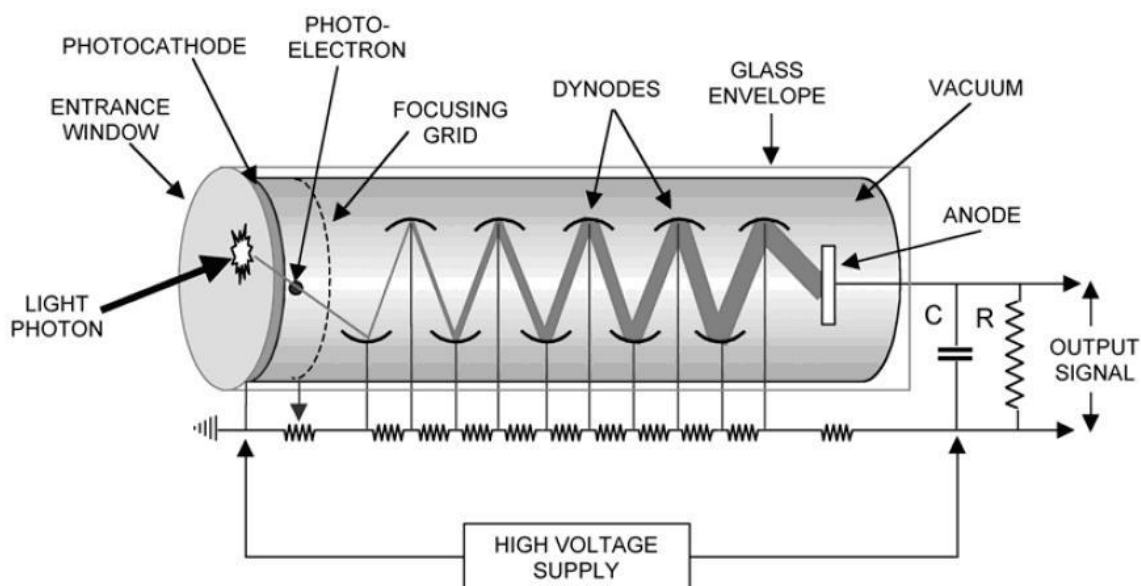


Figure 2.14: PMT System Schematic [2]



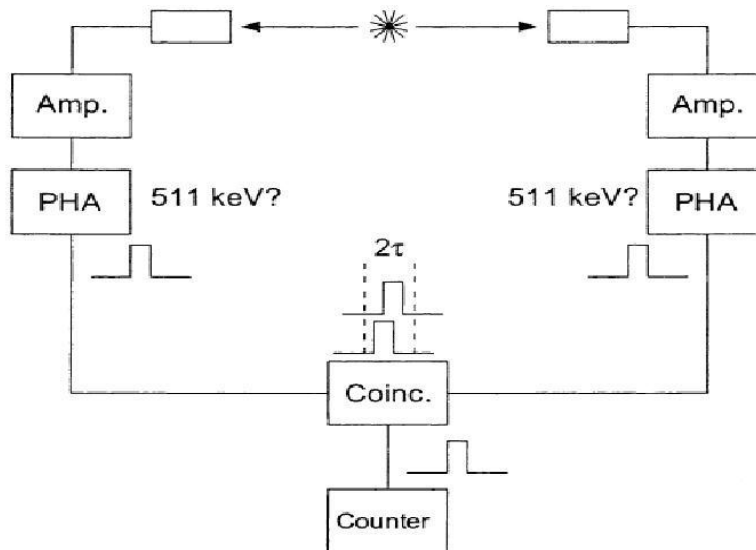


Figure 2.15: Coincidence Circuit [23]

The signal will be amplified and sent to a pulse height analyzer. A logic pulse will be generated and compared to a pulse in the detector in the opposite side. If both pulses are detected within a pulse window with a width of 5-6 ns [5], then a line can be drawn along which the location of positronium must lie and the event is counted as a true coincidence count. Different types of coincidence counts are shown and explained in figure 2.16.

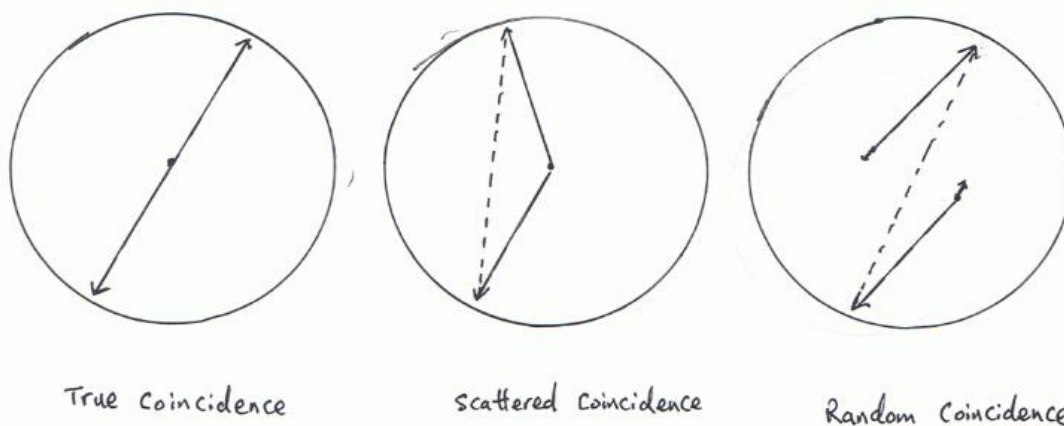


Figure 2.16: Type of Coincidence Counts

## 2.4.2 Image Reconstruction of Algorithm

Theoretically, image reconstruction can be done without the aid of computational algorithms when “time of flight” information can be used to exactly locate the position of annihilation along the line between detectors. However, time of flight information is not available for the MicroPET P4 pre-clinical scanner. Hence, the alternative method is to have image data stored in sinograms or list-mode format, and then to reconstruct the activity field with a mathematical algorithm. Filtered backprojection (FBP) method and iterative reconstruction are two common PET reconstruction algorithms.

## 2.4.3 Filtered Backprojection

Filtered backprojection (FBP) starts with acquiring projection profiles along  $N$  projection angles. A projection profile is defined as the measured radioactivity for all line integrals across from the detectors. An example of projection profile is shown in figure 2.17.

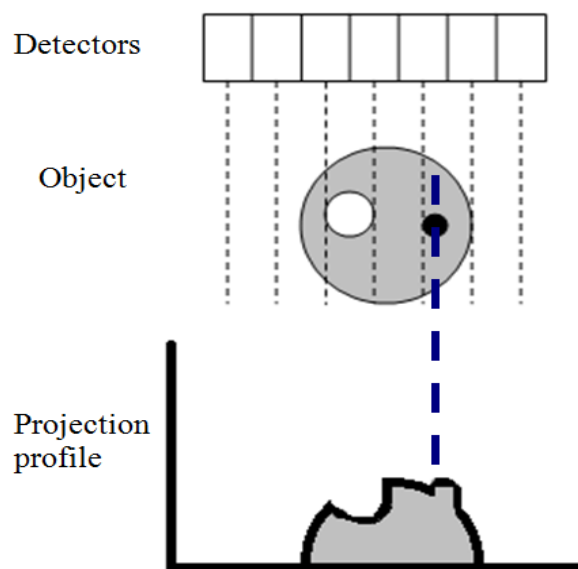


Figure 2.17: Projection Profile

Then a 1-D Fourier transformation (FT) of each profile is computed so everything converts into spatial frequency domain, k-space, as shown in the figure 2.18.

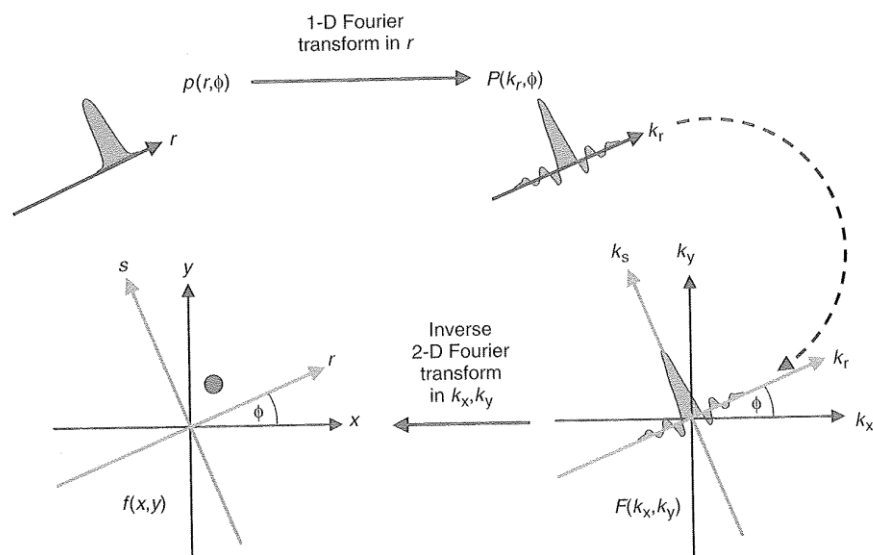


Figure 2.18: Projection of Frequency Domain [5]

$$F(f(x, y)) = F(k_x, k_y) \quad (2.14)$$

$$F(k_x, k_y) = F(k_r, \phi) \quad (2.15)$$

A “ramp filter” applies to each k-space which multiplies each projection FT by  $|k_r|$ . An example of ram filter is shown in figure 2.19.

$$F^*(k_r, \phi) = |k_r| F(k_r, \phi) \quad (2.16)$$

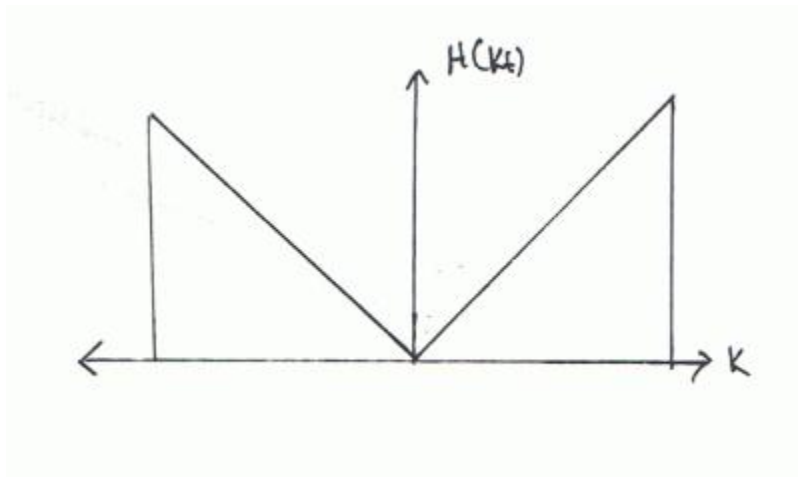


Figure 2.19: The Ramp Filter

Inverse transformation of FT will be computed for each filtered FT profile as shown in equation 2.17.

$$f^*(r, \phi) = F^{-1}(F^*(k_r, \phi)) \quad (2.17)$$

The last step is to re-sum the filtered profiles, as shown in the equation 2.18

$$f(x, y) = \frac{1}{N} \sum_{i=1}^N f^*(x \cos \phi_i + y \sin \phi_i, \phi_i) \quad (2.18)$$

The ramp filter enhances the high spatial frequency and compresses low spatial frequency.

Amplification of high spatial frequency also amplifies the high frequency noise.

However, high frequency noise is rare. One side effect associated with FBP is a ringing effect that is caused by high frequency amplification, which leads to edge-sharpening.

There are many other different filters available for FBP such as Shepp-Logan and Hann for suppression of this artifact [5].

Incomplete data acquisition will result in the object appearing outside of the field of view for certain projections using FBP. The FBP does not account for physical aspects

of the imaging system and data acquisition such as detector spatial resolution and scattered radiation...etc. Lastly, a poor counting statistics can result in a streaked artifact in the image. This artifact may be suppressed with the k-space filter, but this will reduce the spatial resolution within the image. Regardless of these attributes, the FBP algorithms are quick and relatively easy to implement and are frequently used for PET image reconstruction.

### 2.3.4 Iterative Reconstruction Algorithm

The iterative reconstruction algorithm (IRA) is more computation-intensive compared to the FBP. The general concept of IRA is outlined in figure 2.20.

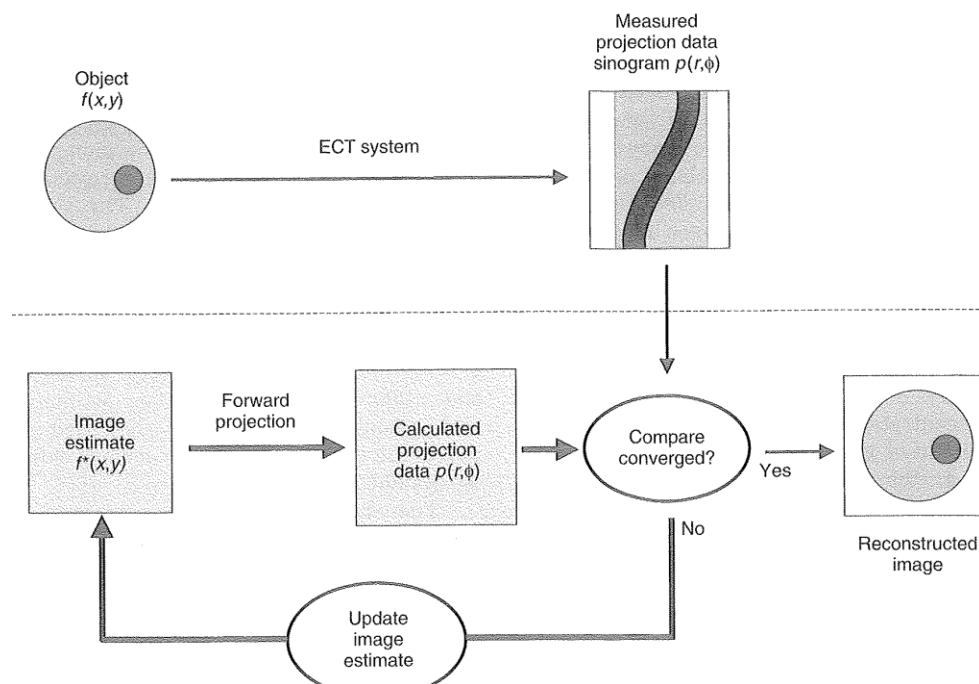


Figure 2.20: Overview of Iterative Image Reconstruction [5]

The goal of IRA is to achieve convergence between the estimated image and recorded image. IRA begins with estimation of the actual image, often a blank or uniform image. The estimated image is then used to compute projections through a process called forward projection. The estimated projection  $f^*(x, y)$  will be compared to the actual measured projection  $f(x, y)$ . The differences between the images are used to update and estimate the image. This process is repeated until the two images reach convergence or fall within a specific convergence range. IRA consists of two basic components: a cost function and a search and update function. The cost function is the method of comparison between the forward projections from the estimated image and recorded projection profiles. The search and update function updates the estimated image base on the cost function output. Some general methods used with IRA to deal with statistical noise include weighting functions and sorting functions and non-negative image reconstruction. The weighting function gives more weight of importance to the high count rate region and lower weight to statistical noise.

Repeating the forward projections process is the most time consuming process for IRA. In comparison to FBP, the backward projection is only computed once during the whole process. IRA accounts for physical characteristics of the imaging device such as system geometry and detector resolution. Although IRAs are much more computationally intensive and time consuming processes compared to FBP algorithms, they have the potential to provide quantitatively more accurate reconstructions.

#### 2.4.4 Expectation-Maximization (EM) Reconstruction

The Expectation-Maximization (EM) is a type of IRA that computes the maximum-likelihood (ML) source distribution, which is also known as the ML-EM method. The statistical weight function is the main component of this algorithm. It assigns greater weight to higher count rate region and lower weight to the lower count rate region. The reconstruction process is governed by equation 2.19.

$$p_j = M_{i,j} a_i \quad (2.19)$$

$M_{i,j}$  is the probability of radiation emitted from the  $i$ th pixel being detected in the  $j$ th,  $p_j$  is the measured intensity in the  $j$ th projection element and  $a_i$  is the intensity (activity) in the  $i$ th pixel in the image. The size of M matrix constructed from the recorded image can be quite large. For instance, in a grid of 128 x 128,  $i$ th and  $j$ th vectors will both run from 1 to 16348. This matrix approach is more accurate compared to the forward projection method. The matrix can be determined through calculation, simulation or a combination of both. Geometry effects, such as symmetry, can also be considered to help reduce the time of constructing the matrix. Once the matrix M is constructed, the intensity pixel value  $a_i$  in the following iteration (k+1) is calculated using the equation 2.20.

$$a_i^{k+1} = \frac{a_i^k}{\sum_j M_{i,j}} * \sum_j M_{i,j} \frac{p_{i,j}}{\sum_i M_{i,j} a_i^k} \quad (2.20)$$

The difference between the k iteration and the (k+1) iterative is measured and used to update the next iteration. The iteration process is terminated when the difference satisfies a pre-determined limit, or after a set number of iterations. The perfect convergence point

where  $a_i^{k+1} = a_i^k$  is impossible to achieve due to existing inaccuracy in the M matrix and statistical noise. ML-EL algorithm is known to produce high quality images with good accuracy.

## 2.5 PET Spatial Resolution Physical Limits

The Positron range, non-colinearity associated with the annihilation process, and the size of detector crystal limit the spatial resolution of a PET system. The size of individual detector elements is very crucial for a detector's spatial resolution. This concept will be demonstrated using a point source. The intrinsic spatial resolution varies with location of the point source. While the point source located at mid-plane, the full width and half max (FWHM) is approximately equal to half of the width,  $d$ , of a detector element. The response profile is triangular in shape. As the point source moves closer to the detector the value of FWHM increases. The shape of the response profile changes to trapezoidal as the source approaches the detector, as illustrated in figure 2.21. The intrinsic resolution,  $R_{int}$ , as a function of the source distance relative to the detector surface is shown in figure 2.21.



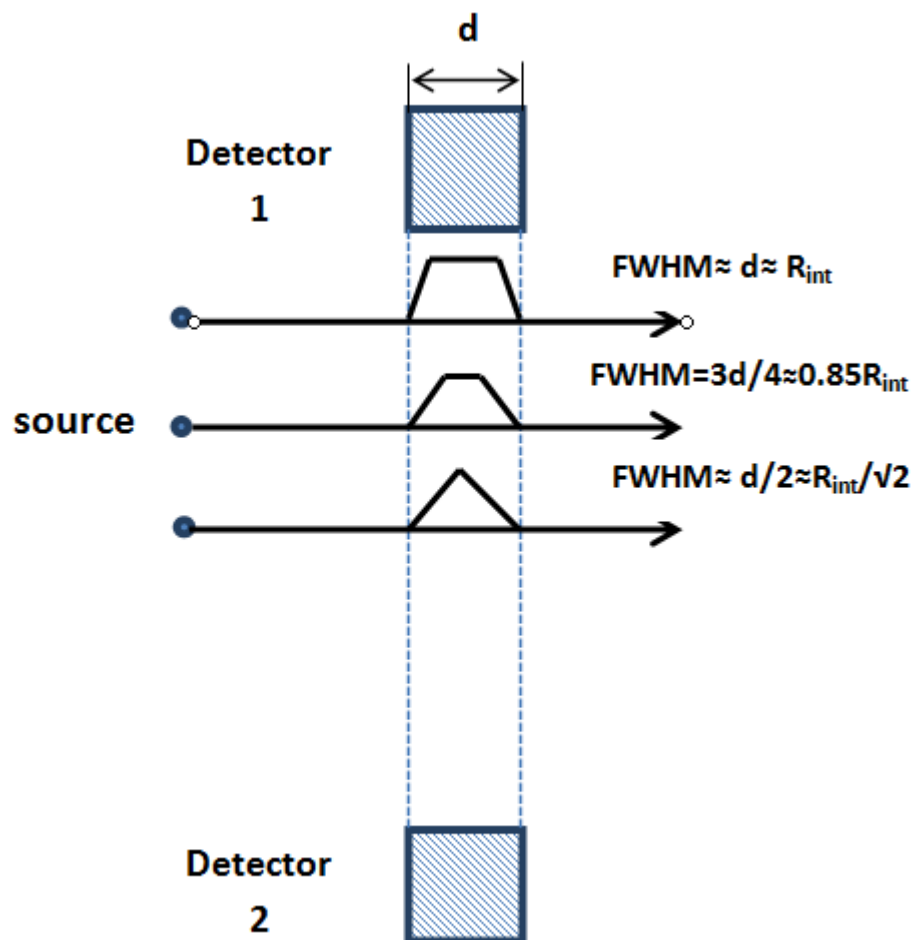


*Figure 2.21: The FWHM as Function of Distance*

Positron range is defined as the distance a positron travels before it undergoes annihilation. A positron behaves like an ordinary electron in that its range can be estimated by that of an electron with the same kinetic energy. The range of a positron in water is approximately same as an electron range with same energy, as shown in figure 2.22.

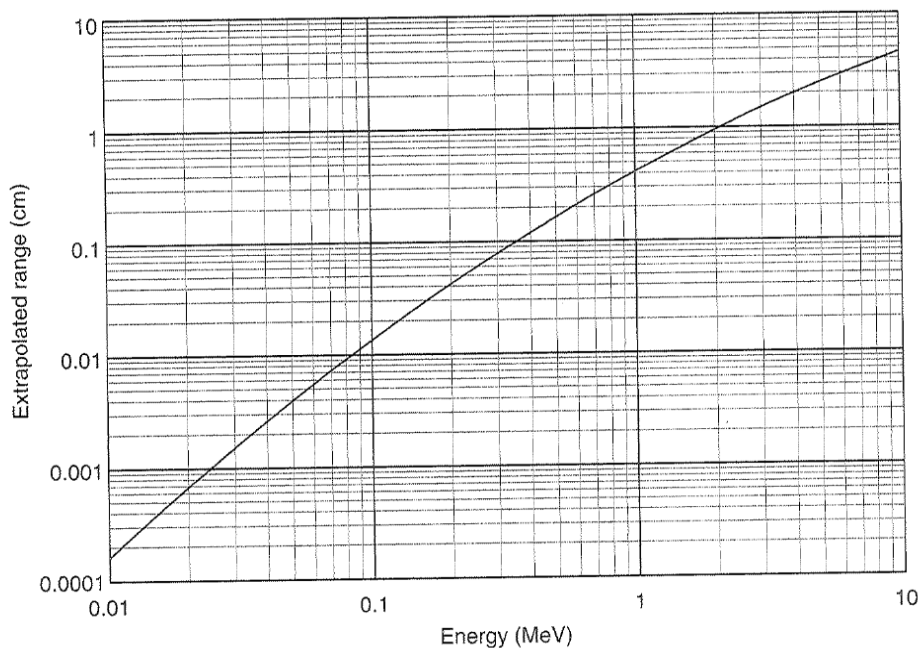


*Figure 2.22: The Electron Range in Water [22]*

The positron loses energy through interaction with surrounding materials, so the path it travels is often of a tortuous shape with large deflection. The average distance a positron travels, from the emitting nucleus to the end of its range prior to annihilation, is called the effective positron range, as shown in figure 2.23. The effective range is always smaller than the extrapolated range. The extrapolated range and the average range for some common beta emitters, beta plus and beta minus emitters, are shown in table 2.4.

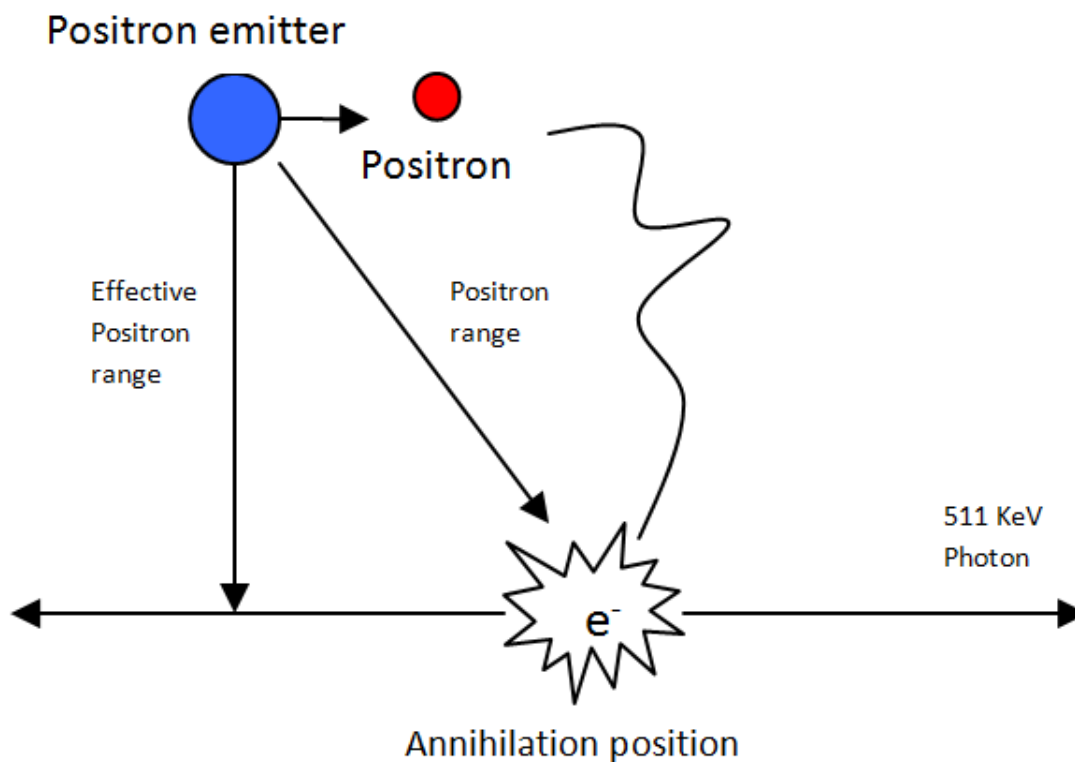


Figure 2.23: The Effective Positron Range

Table 2.4: The Positron Range in Various Materials [5]

Beta-Particle Ranges for Some Commonly Used $\beta^+$ and $\beta^-$ Emitters*					
Radionuclide	$E_{\beta}^{\max}$ (MeV)	Extrapolated Range (cm) in			Average Range (cm) in
		Air	Water	Aluminum	Water
$^3\text{H}$	0.0186	4.5	0.00059	0.00022	—
$^{11}\text{C}$	0.961	302	0.39	0.145	0.103
$^{14}\text{C}^{\dagger}$	0.156	21.9	0.028	0.011	0.013
$^{13}\text{N}$	1.19	395	0.51	0.189	0.132
$^{15}\text{O}$	1.723	617	0.80	0.295	0.201
$^{18}\text{F}$	0.635	176	0.23	0.084	0.064
$^{32}\text{P}$	1.70	607	0.785	0.290	0.198
$^{82}\text{Rb}$	3.35	1280	1.65	0.612	0.429

The extrapolated range for positron emitter F-18 in water is about 2 mm, whereas the FWHM average distribution is about 0.1 mm. The range distribution of a positron can sometimes be non-Gaussian, and may have a fairly long tail. As a result, the root mean

square (RMS) of the effective range is often used instead of FWHM. RMS range for positron emitters in water versus maximum energy is shown in figure 2.24.

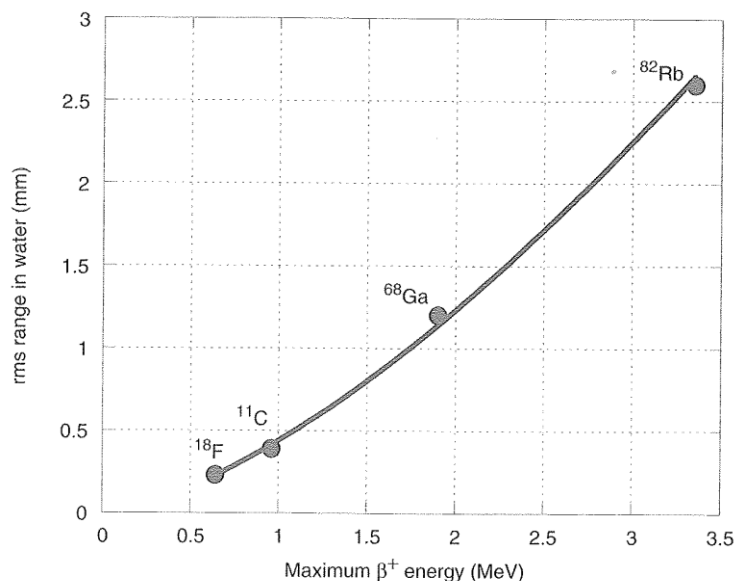


Figure 2.24: RMS Range for Positron in Water [8]

The two gamma rays emitted after the annihilation process are never exactly 180 degrees apart due to variation of residue positron energy at the end of the path. The FWHM distribution is about 0.5 degrees. The non-colinearity response profile relies on separation between the coincidence units, as shown in equation 2.21. For ring detectors, the separation would be the diameter of the rings.

$$R_{180^\circ} = .0022 * D \quad (2.21)$$

The overall system resolution is approximately equal to

$$R_{\text{sys}} \approx \sqrt{R_{\text{det}}^2 + R_{\text{range}}^2 + R_{180^\circ}^2} \quad (2.22)$$

There are many other factors, such as the depth-of-interaction effect, reconstruction filters and data sampling, which can also influence the spatial resolution of the detector system.

## 2.6 Sensitivity

The sensitivity of a PET scanner is determined by the absorption efficiency of the detector system and its solid angle on the object. The true coincidence rate with a source embedded in an absorbing medium is defined as

$$R_{true} = E\varepsilon^2 g_{ACD} e^{-\mu T} \quad (2.23)$$

$E$  is the source emission rate and  $\varepsilon$  is the intrinsic efficiency of each detector. The term  $g_{ACD}$  is the geometric efficiency for coincidence counting detectors. The  $\mu$  is the linear attenuation coefficient and  $T$  is the thickness of the absorbing material.

The intrinsic efficiency is the effectiveness of the detector in capturing counts, which is defined as recorded counts over total emitted gammas. Geometric efficiency for coincidence counting is defined as the fraction of annihilation photons that are emitted in the detector direction that are detected. The maximum geometric efficiency occurs where the source is located at the midpoint between coincidence detectors. The 1D response profile is triangular in shape when the point source is located midway. The 2D response profile has the shape of a pyramid. The average geometric efficiency for a point source located midway between the two detectors is obtained with

$$g_{ACD} \approx \frac{2A_{det}}{3\pi * D^2} \quad (2.24)$$

$D$  is the distance from the detector faces and  $A_{det}$  is the area of the detector facing the source. The factor of 2 accounts for the two detectors for coincidence counting, while the factor of  $1/3$  is the height of the pyramid of the 2D response profile that is the average geometric efficiency across the sensitive volume.

As for a typical stationary ring scanner, each detector element is operating in coincidence with multiple detectors on the opposite side as shown in figure 2.25.

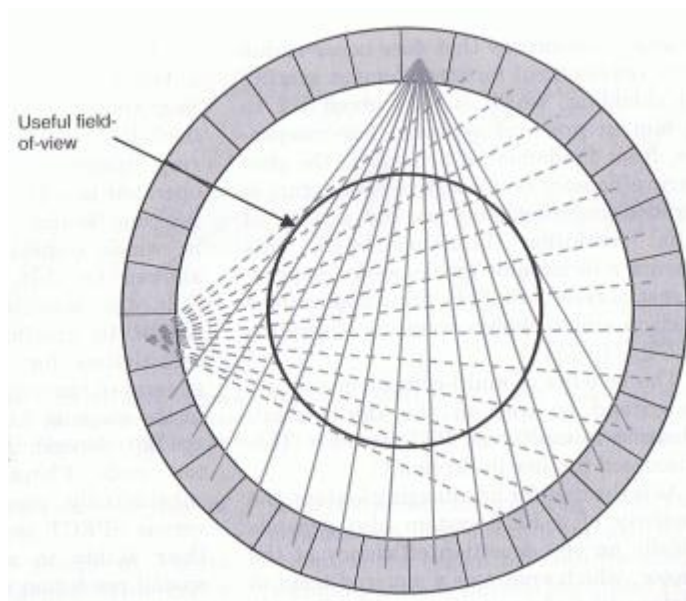


Figure 2.25: Coincidence Counting with Multiple Crystals [5]

The geometric efficiency for a ring detector is dependant on the scanner diameter,  $D$ .

The detector element size,  $d$ , is assumed to be much smaller than the scanner diameter.

The axial thickness is defined as  $h$  in this case. Also, gaps between the adjacent detector

elements are assumed to be insignificant. The geometric efficiency for a ring scanner

with a source located in the center of the ring can be approximated with the equation 2.25.

$$g_{ACD,ring} \approx \frac{h}{D} \quad (2.25)$$

The geometric efficiency remains fairly constant as the source moves away from the center of the ring while remaining in the center plane. As the source moves to the end plane position, the solid angle of the geometric efficiency has a triangular shape. Hence, the average geometric efficiency for a source within the sensitive volume and near the vicinity of the center of the ring is defined as

$$\overline{g_{ACD,ring}} \approx \frac{h}{2D} \quad (2.26)$$

Simultaneous acquisition of multiple projection views without moving the detectors is one advantage of the stationary ring shaped scanner. A typical ring scanner uses parallel beam profiles to acquire projection as shown in figure 2.26.

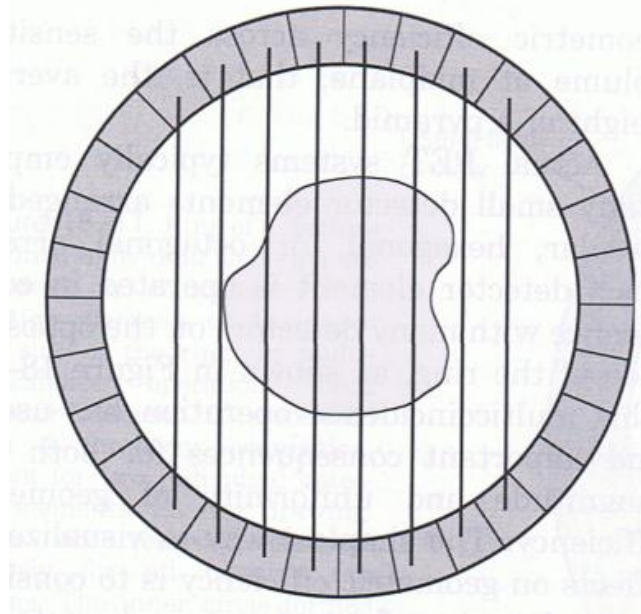


*Figure 2.26: The Parallel Beam Profile [5]*

The number of projections needed to obtain the complete image is one fourth of the total number of detectors in the ring. This reduces the amount of time needed to acquire a

PET image and is much faster than the rotational type scanner. A PET image capture time is also dependent on the detection efficiency of the detectors. The detector efficiency is defined as

$$\varepsilon = 1 - e^{-\mu x} \quad (2.27)$$

The linear attenuation coefficient is denoted by  $\mu$  and  $x$  is the detector thickness. The linear attenuation and detection efficiencies for common scintillators at 511 keV can be found in table 2.5.

Table 2.5: The Linear Attenuation and Detection Efficiencies [5]

Linear Attenuation Coefficients and Detection Efficiencies for Some Scintillators at 511 keV*					
Scintillator	$\mu$ (511 keV) $\text{cm}^{-1}$	$\varepsilon$ (2 cm) <sup>†</sup>	$\varepsilon^2$ (2 cm)	$\varepsilon_{50}$ (2 cm) <sup>‡</sup>	$\varepsilon_{50}^2$ (2 cm)
NaI(Tl)	0.34	0.49	0.24	0.25	0.061
BGO	0.95	0.85	0.72	0.43	0.18
LSO	0.88	0.83	0.69	0.41	0.17
GSO	0.70	0.75	0.57	0.38	0.14
BaF <sub>2</sub>	0.44	0.58	0.34	0.29	0.086

\*Efficiency values are for 2-cm thick crystals.

The detection efficiency for a pair of coincidence counting detectors is listed under column  $\varepsilon^2$  since there are two detectors used. For LSO crystals, the linear attenuation is about 0.88 per cm and detection efficiency is about 0.69.

## 2.7 PET Data Correction

There are four common data corrections used in PET: normalization, correction for random coincidence, scattered radiation correction and attenuation correction. Small variations in PET component, such as the size of the crystal during the manufacturing process, are inevitable. These variations disrupt the consistency and accuracy of the scanner. Normalization is one of the most common methods used to account for



variations in the scanner's components. The basic normalization approach is to measure counts for each pair of coincidence detectors using a libration source. The recorded counts will be divided by an average number of counts to obtain the normalization factor. For future imaging practices using the same PET scanner, the normalization factor will be multiplied by the recorded counts for each pair of detectors. Then, PET images can be reconstructed with the corrected counts.

Random coincidences often add a uniform layer of background to the image that reduces contrast within the image. This problem is often dealt with using a delay window. Basically, a PET scanner is designed to determine the validity of a coincidence count based on the photon arrival time. If two photons arrive within a predefined coincidence timing window (CTW), typically 6-12 nanoseconds, then it will be record as a valid event. The delay window is set at a much later time and has much greater window width compared to regular CTW. Any coincidence counts recorded within the delayed window provide an estimated count of random events. The true coincidence count can be estimated by the difference between the total recorded coincidence events in the CTW and the counts recorded in the delay window. However, subtracting the random coincident count may increase the statistical noise level in the image.

The scattered radiation has a great effect on PET image quality; it reduces the image contrast and increases ambiguity between activity and pixel intensity. In 3D PET imaging, scattered counts are majority of the counting statistic, sometimes accounting for 60-70% of the total number of counts [5]. For a coincidence event, it is necessary to count two photons as one valid event, which makes the event more susceptible to the

scatter effect. Statistically, counting two photons as one event has a higher scatter probability when compared to counting a single photon using SPECT. PET scanners commonly use LSO and BGO crystals as a scintillator. These crystals have a lower light output compared to NaI crystals. In order to capture an un-scattered event, a wider pulse-height analyzer is used to compensate for the lower light output. The photon's predominant mode of interaction in the scintillator is the Compton scattering. Even if an un-scattered photon enters the scintillator it is very rare that all 511keV of energy is deposited in the crystal. It is impossible to determine whether the location of the scattered event is in the image volume or the scintillator.

There are two main methods used in PET for scatter correction. The first method is to derive a correction factor from an image containing the scatter effect and a transmission image. The transmission image maps attenuation coefficients within the subject of interest. An attenuation map can be used to estimate the distribution of scatter events and their contributions to the image. The estimated scattered distribution can be subtracted from the original image to obtain the filtered image. This method works when all activities are contained within the field of view, but it is relatively more computationally intensive. For medical imaging practices, an examination of the projection profile outside of the object is a quick method for scatter correction. The scattered distribution can be estimated with a simple smoothing function, such as the cosine function or the Gaussian function. This method is quicker because it only accounts for scattered events outside of the field of view. If the subject of interest is laid completely within the field of view, then this method is invalid.

The attenuation correction is the most common correction used in PET imaging. The attenuation correction can be done with information from a blank scan and transmission scanner. The attenuation factor can be calculated using estimated information from a blank scan and transmission scan. Postinjection transmission scanning is an alternative method. This method involves a transmission scan while the tracer remains in the subject immediately following the emission scan. The postinjection method can increase the accuracy and also reduce the chance of patient motion and misalignment. The simultaneous emission and transmission scanning is available on some medical scanners. It is an attenuation correction method that known to be the most effective.

## Chapter 3

### Fundamental Fluid Dynamics

#### 3.1 Flow Characteristic and Boundary Layer

For fluid flow over a solid stationary boundary or wall, the fluid velocity between the fluid and the wall surface is zero. Under “no slip” or continuous flow conditions, the velocity gradient is developed in the direction that is normal to the flow. The velocity gradient is created by wall shear force  $\tau_x(y)$  acting on the surface of an element, as shown in figure 3.1.

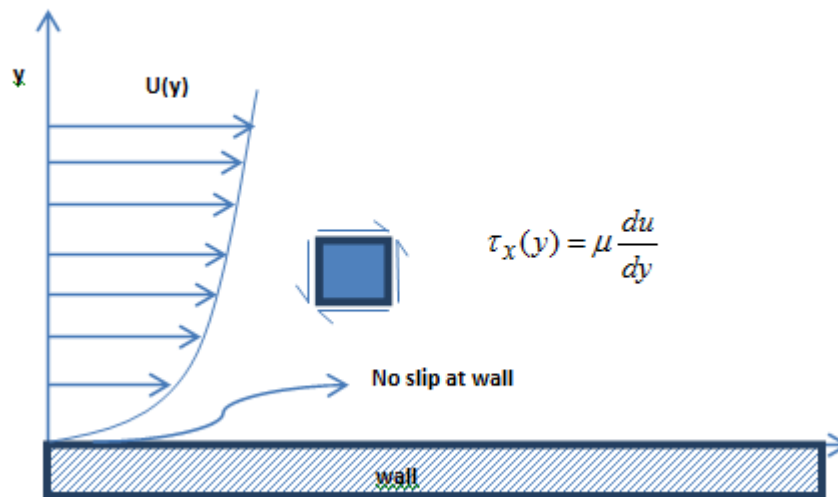


Figure 3.1: Shear Force

The shear force on the bottom surface slows down the element, while the force on the top surface moves the element in the direction of flow. The distance between two surfaces is proportional to the velocity difference between the top and bottom of the element. For

Newtonian fluids, shear force can be described with dynamic viscosity  $\mu$ , shown in equation 3.1.

$$\tau_x(y) = \mu \frac{du}{dy} \quad (3.1)$$

If the flow is moving at a constant velocity  $U$  over a boundary surface with length  $L$ , the shear force is greatest at the wall; the relative velocity between the flow and the wall is zero. As an element moves away from the wall, the flow velocity varies from 0 to  $0.99U$ . The thickness of the boundary layer normal to the plate varies in the  $x$  direction, and is denoted by  $\delta$ . The complete boundary layer is shown in figure 3.2

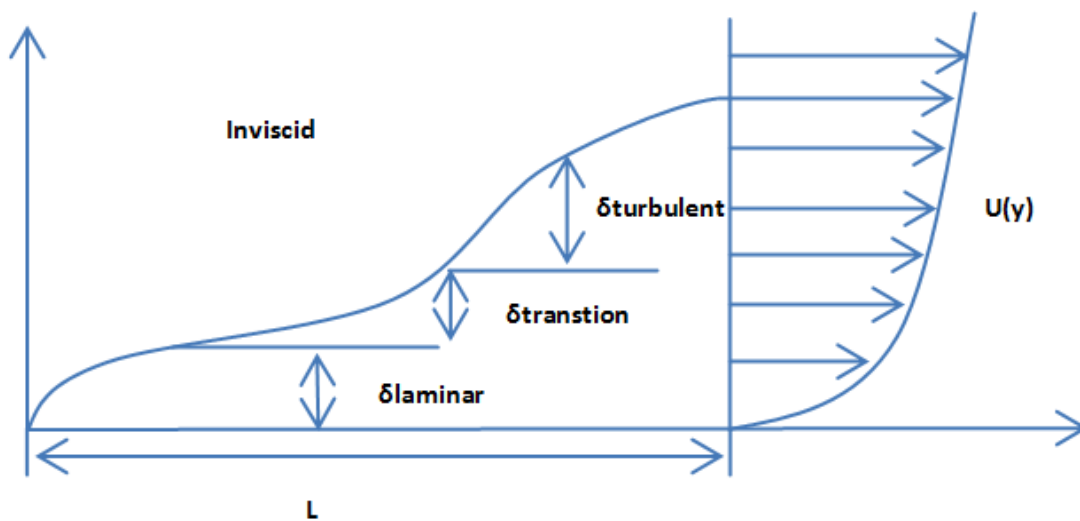


Figure 3.2: Boundary Layer

The boundary layer is often divided into three flow regimes: the laminar flow regime, the transition flow regime and the turbulent flow regime. Flow regimes are often characterized by the dimensionless Reynolds number. It is denoted by  $Re$ , which

represents the ratio of inertial force on a fluid over the viscous force, as shown in equation 3.2.

$$\text{Re} = \frac{UL_c}{\nu} \quad (3.2)$$

Characteristic length  $L_c$  is used to calculate the Reynolds number.

### 3.2 Internal Flows

Internal flow describes flow within a completely enclosed solid boundary, such as a pipe or duct. The boundary layer for internal flow is similar to the external flow boundary described in the preceding section. The major difference between the two is the velocity gradient exists on all enclosed surfaces. Velocity gradients merge in the center of the duct where the flow development approaches a point where the thickness of the boundary layer merges at the flow centerline. The velocity gradient changes as fluid moves away from the inlet and slowly approaches the fully developed stage. Entrance length  $L_e$  is defined as the distance from the inlet in the flow direction where the velocity profile becomes stable and consistent. The entrance length is dependant on the wall roughness. The entrance length [17] for laminar flow and turbulent flow can be estimated with the equations below.

$$L_e = 0.060(d)\text{Re} \quad \text{for laminar flows} \quad (3.3)$$

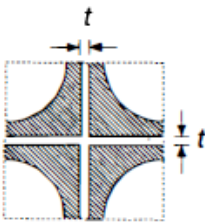
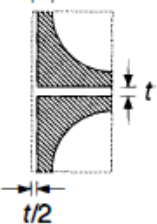
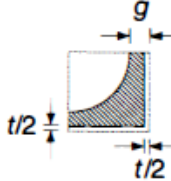
$$L_e = 4.40(d)\text{Re}^{1/6} \quad \text{for turbulent flows} \quad (3.4)$$

The Reynolds number calculation is slightly different for internal flow which is shown in equation 3.5.

$$\text{Re} = \frac{V^* d_h}{\nu} \quad (3.5)$$

Hydraulic diameter is denoted by  $d_h$ . For a circular pipe, it is equal to the diameter of the pipe. For non-circular pipes, it is equal to 4 times the cross sectional area over the wetter perimeter. A square array nuclear fuel bundle, such as that considered in figure 1.1 makes the area and the wetted perimeter calculation somewhat complicate. The cross sectional area for flow is the opening area between fuel rods and spacers. Table 3.1 provides formulas for evaluation of the cross sectional area and the wetted perimeter in square fuel bundle.

Table 3.1: Square Array Hydraulic Area and Wetted Perimeter Evaluation [19]

	$i = 1$ INTERIOR	$i = 2$ EDGE	$i = 3$ CORNER
Area			
$A_{fi}$ (area for flow without spacer)	$P^2 - \frac{\pi D^2}{4}$	$P \left( \frac{D}{2} + g \right) - \frac{\pi D^2}{8}$	$\left( \frac{D}{2} + g \right)^2 - \frac{\pi D^2}{16}$
$A_{fi}$ (average area for flow with spacer)	$A_{fi} - (2Pt - r^2)\delta$	$A_{fe} - \left[ \left( \frac{D}{2} + g - r^* \right) t + \frac{Pt^*}{2} \right] \delta$	$A_{fc} - \left[ 2 \left( \frac{D}{2} + g \right) r^* - r^{*2} \right] \delta$
$P_{wi}$ (wetted perimeter without spacer and duct)	$\pi D$	$\frac{\pi}{2} D$	$\frac{\pi}{4} D$
$P_{wi}$ (average wetted perimeter including spacer but without duct)	$\pi D + 4(P - r)\delta$	$\frac{\pi}{2} D + \left[ \left( \frac{D}{2} + g - r^* \right) 2 + (P - r) \right] \delta$	$\frac{\pi}{4} D + \left( \frac{D}{2} + g - r^* \right) 2\delta$

The overall average hydraulic diameter can be evaluated with formulas from table 3.2.

Table 3.2: Average Hydraulic Diameter Evaluation [19]

---

Assuming grid spacer around  $N_p$  rods of thickness  $t$  and that  $g = \frac{P - D}{2}$

1. Total area inside square ( $A_T$ ):

$$A_T = D_\ell^2$$

where  $D_\ell =$  length of one side of the square.

2. Total average cross-sectional area for flow ( $A_{fT}$ ):

$$A_{fT} = D_\ell^2 - N_p \frac{\pi}{4} D^2 - N_p \frac{t}{2} P 4\delta + N_p \left(\frac{t}{2}\right)^2 4\delta$$

$$A_{fT} = D_\ell^2 - \left[ N_p \frac{\pi}{4} (D^2) + 2\delta(\sqrt{N_p})(D_\ell t) - N_p t^2 \delta \right]$$

because  $D_\ell = \sqrt{N_p} P$  and  $t^* = t$

where:

$D =$  rod diameter  
 $N_p =$  number of rods  
 $t =$  interior spacer thickness  
 $t^* =$  peripheral spacer thickness

3. Total average wetted perimeter ( $P_{wT}$ )

$$P_{wT} = N_p \pi D + 4\sqrt{N_p} D_\ell \delta - 4N_p t \delta$$

4. Equivalent hydraulic diameter for overall square ( $D_{eT}$ )

$$D_{eT} = \frac{4 A_{fT}}{P_{wT}} = \frac{4 D_\ell^2 - [N_p \pi D^2 + 8\sqrt{N_p} D_\ell t \delta - 4N_p t^2 \delta]}{N_p \pi D + 4\sqrt{N_p} D_\ell \delta - 4N_p t \delta}$$


---

The Reynolds number [15] that describes the transition point between laminar and turbulent internal flow is approximately 2300. The fully turbulent region is laid beyond the Reynolds number value 4000.

The laminar flow has a lower Reynolds number where viscous forces dominate. In turbulent flow, element dispersion or mixing occurs due to random and fluctuation turbulence. Different flow regimes are shown in figure 3.3.



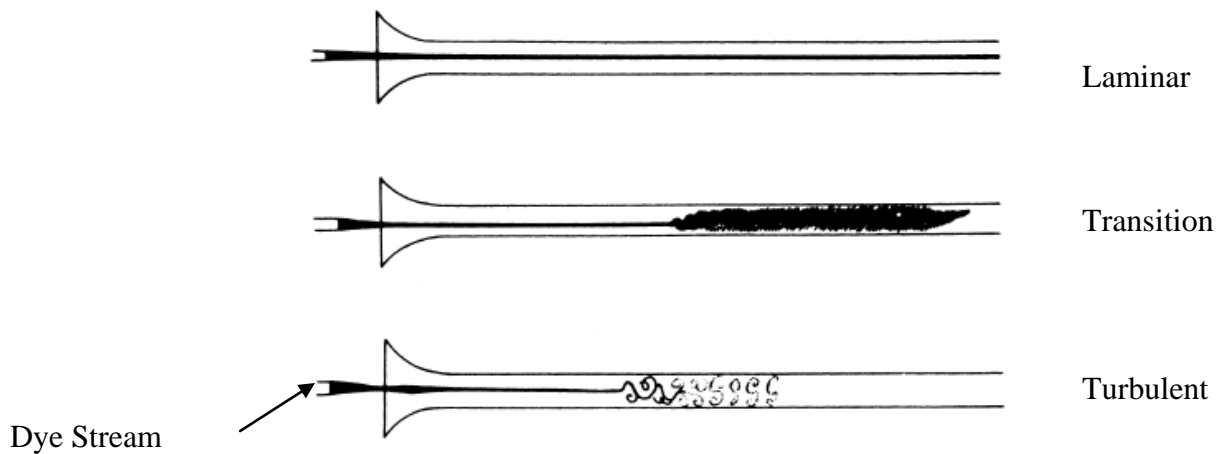


Figure 3.3: Different Flow Regimes [18]

### 3.3 Fickian Diffusion

Diffusion is a fundamental transport process that involves the movement of concentration from high concentration to low concentration in a very random nature. The diffusion process occurs in a nature that obeys the Fickian diffusion laws. Fick's first law is defined as

$$q_{\nabla} = -D\nabla C = -D\left(\frac{dC}{dx} + \frac{dC}{dy} + \frac{dC}{dz}\right) \quad (3.6)$$

The diffusive flux  $q_{\nabla}$  is the amount of mass elements per unit area per unit time, and is proportional to the concentration gradient  $\nabla C$ .  $C$  has units of mass per unit volume. The diffusion coefficient  $D$  has a unit of length<sup>2</sup>/time. For a one dimensional case, the diffusion equation in the  $x$  direction is shown below.

$$q_x = -D\frac{dC}{dx} \quad (3.7)$$

Fick's second law is defined as the rate of change in concentration over time, as shown in equation 3.8

$$\frac{\partial C}{\partial t} = -D\nabla^2 C = -D\left(\frac{d^2 C}{dx^2} + \frac{d^2 C}{dy^2} + \frac{d^2 C}{dz^2}\right) \quad (3.8)$$

As for a one dimensional case,  $\frac{d^2 C}{dy^2} = \frac{d^2 C}{dz^2} = 0$ .

### 3.4 Advective Diffusion Process

In a fluid transport situation, the diffusion process is a combination of advection and diffusion. A stationary advective diffusion process with a stationary source with a flow velocity  $u$  in the control volume is shown in figure 3.4

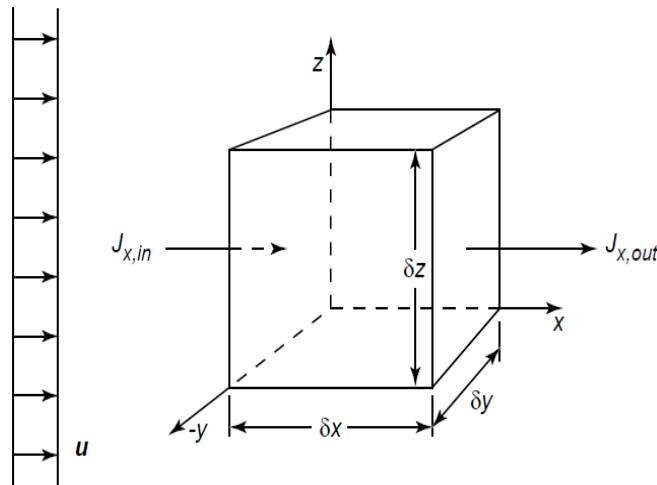


Figure 3.4: The Control Volume [18]

The net movement of a fluid element in this situation includes flow and molecular motion.

The total flux  $J_x$  in the  $x$  direction is shown in equation 3.9.

$$J_x = uC + q_x = uC - D\frac{\partial C}{\partial x} \quad (3.9)$$

The advective diffusion equation can be derived from the conservation of mass in the x,y and z directions in a control volume.

$$\frac{\partial M}{\partial t} = \sum \dot{m}_{in} - \sum \dot{m}_{out} \quad (3.10)$$

For the x direction, the mass flow rate  $\dot{m} = J_x * \delta y \delta z$  (3.11)

Substitute equation 3.11 into conservation of mass in the x direction,

$$\delta \dot{m} \Big|_x = (uC - D \frac{\partial C}{\partial x}) \Big|_1 \delta y \delta z - (uC - D \frac{\partial C}{\partial x}) \Big|_2 \delta y \delta z \quad (3.12)$$

Equation 3.12 can be further simplified

$$\delta \dot{m} \Big|_x = - \frac{\partial(uC)}{\partial x} \delta x \delta y \delta z + D \frac{\partial^2 C}{\partial x^2} \delta x \delta y \delta z \quad (3.13)$$

The  $\vec{u}=(u,v,w)$  is a velocity vector in x, y and z directions, the sum of mass in all direction is

$$\begin{aligned} \delta \dot{m} \Big|_{x,y,z} &= - \frac{\partial(uC)}{\partial x} \delta x \delta y \delta z + D \frac{\partial^2 C}{\partial x^2} \delta x \delta y \delta z - \frac{\partial(vC)}{\partial y} \delta x \delta y \delta z + \dots \\ &\dots D \frac{\partial^2 C}{\partial y^2} \delta x \delta y \delta z - \frac{\partial(wC)}{\partial z} \delta x \delta y \delta z + D \frac{\partial^2 C}{\partial z^2} \delta x \delta y \delta z \end{aligned} \quad (3.14)$$

M is equal to  $C \delta x \delta y \delta z$ , and can be used to further simplify equation 3.14.

$$\frac{\partial C}{\partial t} \Big|_{x,y,z} = - \frac{\partial(uC)}{\partial x} + D \frac{\partial^2 C}{\partial x^2} - \frac{\partial(vC)}{\partial y} + D \frac{\partial^2 C}{\partial y^2} - \frac{\partial(wC)}{\partial z} + D \frac{\partial^2 C}{\partial z^2} \quad (3.15)$$

The final advective diffusion equation is obtained as

$$\frac{\partial C}{\partial t} \Big|_{x,y,z} = -\nabla \cdot (\vec{u}C) + D \nabla^2 C \quad (3.16)$$

During the advective diffusion transport process, there may be one dominate transport method, either diffusive or advective. The dominant transport method can be determined with the Peclet Number, which is denoted by  $Pe$ . The Peclet Number is shown in equation 3.17.

$$Pe = \frac{D}{u^2 t} \quad (3.17)$$

When  $Pe \gg 1$ , the diffusion process is dominant which means the cloud diffuses faster than the bulk moving speed. As  $Pe \ll 1$ , the cloud diffuses slower than the bulk moving speed [18].

### 3.5 Turbulence Advective Diffusion Equation

The advective diffusion process gets more complicated due to turbulence effects. Turbulent flow is highly unsteady and includes random eddies. The kinetic energy in the flow creates eddies with larger eddies breaking into multiple smaller eddies. The energy transfer from larger eddies to small eddies is very efficient so relatively little energy is lost [17]. Eventually the small eddies disappear due to viscous dissipation, and the turbulent kinetic energy is converted to heat, which is called dissipation. Flow fluctuates with time in the turbulent flow regime as shown in figure 3.6. Eddies in an advective diffusion process increase the diffusion effect within the flow.

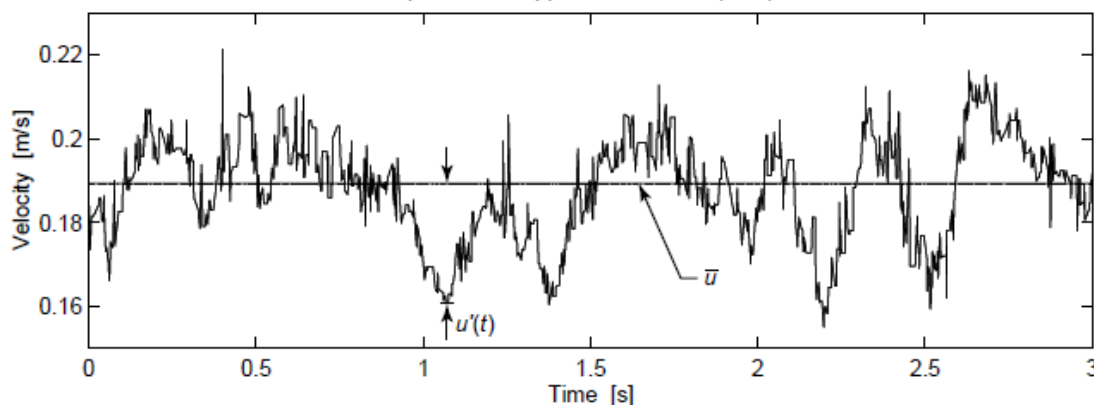


Figure 3.5: Turbulent Velocity Fluctuation [18]

It is very difficult to predict the location and velocity of a fluid element later in time in the turbulent flow. The velocity prediction is often done using Reynolds decomposition.

$$u_i(x_i, t) = \bar{u}_i(x_i) + u_i'(x_i, t) \quad (3.18)$$

$\bar{u}_i(x_i)$  is the mean velocity and  $u_i'(x_i, t)$  is the fluctuation. The analogy method is applied to the concentration and time averaged flux shown in equation 3.19 and equation 3.20.

$$C(x_i, t) = \bar{C}(x_i) + C'(x_i, t) \quad (3.19)$$

$$q_x = \overline{(u_i(x_i) + u_i'(x_i, t))(\bar{C}(x_i) + C'(x_i, t))} = \overline{u_i \bar{C}} + \overline{u_i C'} + \overline{u_i' \bar{C}} + \overline{u_i' C'} \quad (3.20)$$

With a homogenous flow, the fluctuation  $u_i'$  and the concentration  $C'$  are zeros shown in equation 3.22 and 3.23.

$$q_x = \overline{u_i \bar{C}} + \overline{u_i' C'} \quad (3.21)$$

$$\overline{u_i'} = \frac{\int_t^{t+T} u_i' dt}{T} = 0 \quad (3.22)$$

$$\overline{C_i'} = \frac{\int_t^{t+T} C_i' dt}{T} = 0 \quad (3.23)$$

Then by substituting Reynolds' decompositions into the equation 3.16 and integrating from (t to t+T) as function of time, the turbulent advective diffusion equation is obtained as

$$\frac{\partial \overline{C}}{\partial t} + \overline{u_i} \frac{\partial \overline{C}}{\partial x_i} = - \frac{\partial \overline{u_i' C_i'}}{\partial x_i} + - \frac{\partial}{\partial x_i} (D \frac{\partial \overline{C}}{\partial x_i}) \quad (3.24)$$

There is one problem remaining in this equation in that the mass flux  $\overline{u_i' C_i'}$  needs to be defined. From Rutherford and Fischer studies [18], it shown the mass flux is analogous to molecular diffusion.

$$\overline{u_i' C_i'} = D_i \frac{\partial \overline{C}}{\partial x_i} \quad (3.25)$$

$$D_i = \frac{(\Delta x)^2}{\Delta t} = u_T l_T \quad (3.26)$$

This model only valid for  $\Delta t \gg T$ , if  $\Delta t = T$ , the average turbulent diffusion length scale is equal to  $\Delta x = u_T t_T = l_T$ . The final turbulent advective diffusion equation is shown in equation 3.27. Turbulent diffusion  $D_i$  is generally much greater than molecular diffusion,  $D_m$  [18].

$$\frac{\partial \overline{C}}{\partial t} + \overline{u_i} \frac{\partial \overline{C}}{\partial x_i} = - \frac{\partial}{\partial x_i} (D_i \frac{\partial \overline{C}}{\partial x_i}) + - \frac{\partial}{\partial x_i} (D_m \frac{\partial \overline{C}}{\partial x_i}) \quad (3.27)$$

The modeling approach offered by Rutherford and Fisher is not adequate for many engineering situations. The modeling of flow turbulence such that diffusion of enthalpy and concentration is properly predicted in engineering flows remains an area of active research. A simulation of flow is presented later that uses advective diffusion models in COMSOL to predict flow diffusion measurement using PET.

## Chapter 4

### Experiment using PET to Image Flow Mixing

This chapter will demonstrate the methodology of incorporating PET into one phase flow studies. The experiment design and setup are discussed in detail in this chapter. Pre-experiment preparations such as radiation shielding efforts are also addressed. A CFD simulation was made in the COMSOL code as an example for validation purposes.

#### 4.1 Experiment Design

To incorporate PET into fluid flow studies, there are many challenges. The first challenge is the water-soluble nature of the scintillation crystals in the PET scanner. The test section must be completely sealed and leak proof. The second challenge is the PET scanner's 0.08 m axial field of view. The tracer only remains inside the field of view for a very short period of time. MicroPET P4 is the PET scanner used for this study, the system specifications can be found in chapter 2. MicroPET P4 has an axial field of view of approximately 8 cm. For a particle traveling with a relatively low velocity of 1 m/s, it will remain under the P4's field of view for less than a tenth of a second. The third challenge is associated with radiation shielding for the high activity of PET tracer. The effective and controlled delivery of the radiation with minimal exposure requires planning and rehearsal.



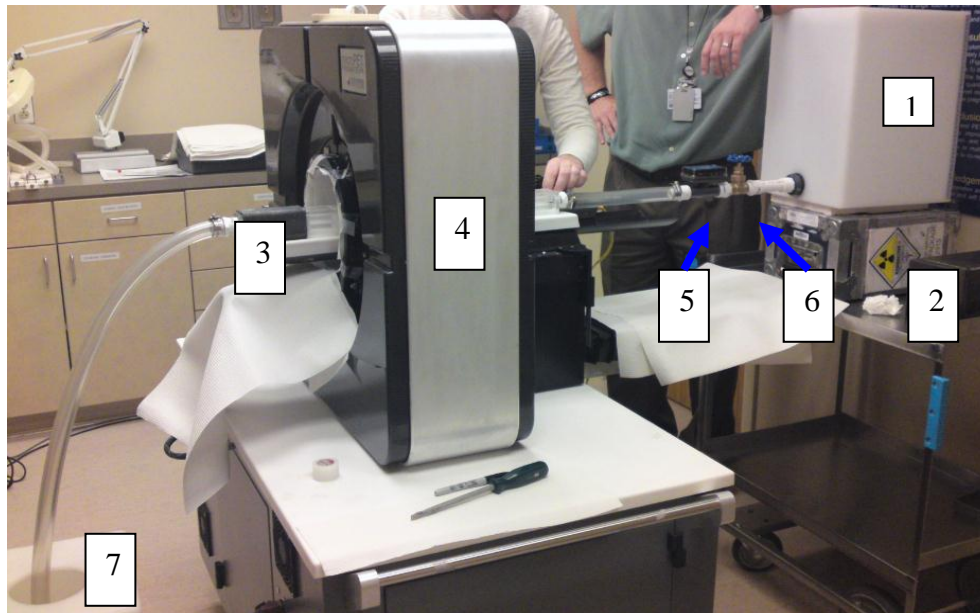


Figure 4.1: The 1<sup>st</sup> Experiment Setup: 1. Header Tank; 2. Shielding Box; 3. Test Section; 4. P4 PET Scanner; 5. Turbine Meter; 6. Globe Valve; 7. Storage Tank.

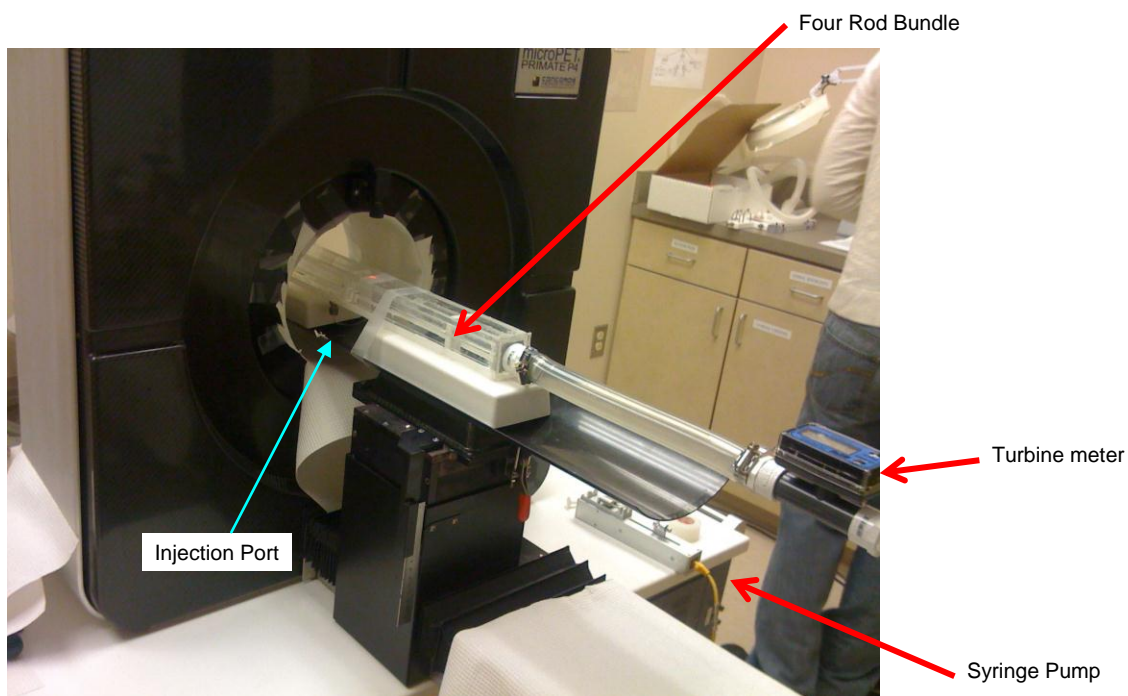
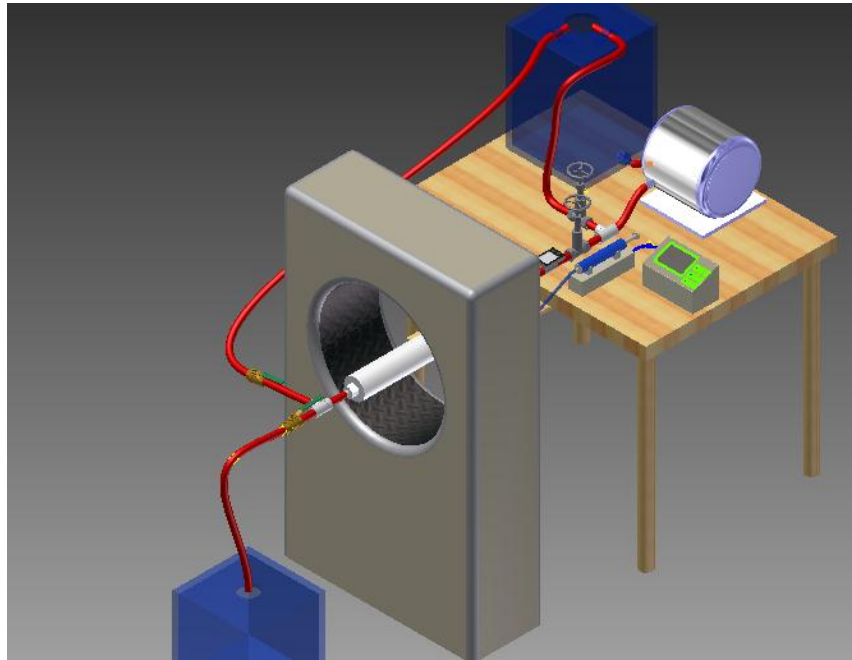


Figure 4.2: Closer View of Experiment Setup

This design is fairly simple, but addresses major design constraints. The water loop is designed to be a once-through cycle. Water in the water tank (1) is transfer into the test section (3). As water flows through the test section, PET tracer is injected into the test section. The injection process is handled with a remote controlled syringe pump. The PET tracer is stored in a small volume syringe and delivered to the test section using butterfly injection tubing. The syringe pump is placed in a lead or steel shielding box (2). This setup minimizes the radiation exposure and ensures a consistent injection rate. As the tracer passes through the test section of interest, the PET scanner (4) is able to collect the radiation counts needed to assemble an image. The fluid flow rate reading is available on the turbine meter (5). The flow rate can be controlled with a globe valve or ball valve (6). The water with PET tracer is dumped into a storage tank (7). The storage tank will remain in the experiment room untouched until all the radioactive tracer decays. The F18 PET tracer has a 110 minute half-lives that allow decay to below background activity level within a couple of days. With this setup, the major radiation exposure time is reduced to the time needed to set up the syringe pump and place it in the shielding box. One drawback of this design is the loading process of the syringe pump system may take longer than desired.

The experiment design is improved after two preliminary tests, which will be discussed in more detail in the next section. The second generation experiment facility design is shown in figure 4.3.



*Figure 4.3: Improved Experiment Design*

The major differences are the shielding box is removed and a recirculation loop is added. Without a shielding box, the process of loading the syringe and setting up the system is expedited. This greatly reduces radiation exposure time. The recirculation loop allows the test section to be filled and tested prior to tracer injection. In addition, a web-camera is added to record the flow rate reading during the experiment. The experimental facility is otherwise similar to the initial experimental design.

#### **4.2 2X2 Test Section**

The first test section was a 2x2 fuel bundle geometry test section. The test section is shown in the figure 4.4 and 4.5.

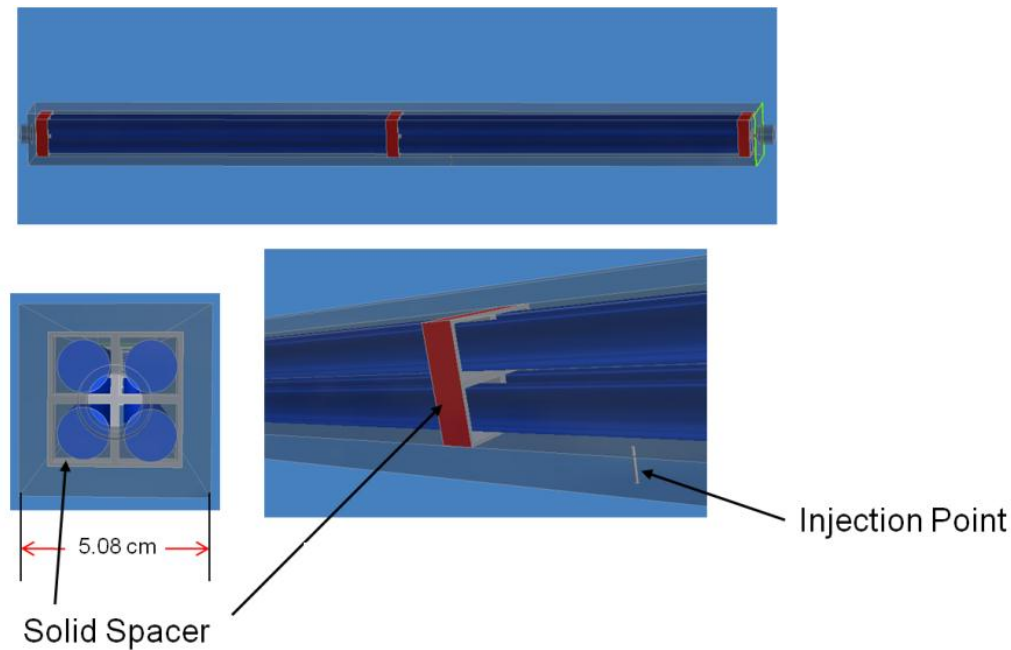


*Figure 4.4: A 2X2 Square Array Test Section.*



*Figure 4.5: The 2X2 Test Section*

It is approximately 61 cm long with a square cross section of side length 5.08 cm. The test section encases four 1.27 cm acrylic rods held by three solid spacers. The injection point is designed to be 31.8 cm from the inlet and 3.18 cm from the second spacer. The injection point is between the boundary wall and the acrylic rod, which is approximately 0.4 cm from the wall.

This test section was used in the first two tests using PET for fluid flow studies. The experimental parameters are very similar for these two experiments. The PET tracer is F-18 in the form of FDG solution. The flow rate is designed to produce Reynolds number of approximately 1500. The Reynolds number calculations for the square array fuel bundle are available in Appendix A. The first generation experiment setup used for these tests used gravity drain to produce the flow rate.

A low Reynolds number is chosen to accommodate the set radiation activity limit of 50 mCi, which is the maximum hand carried activity. It was not known if this level of radioactivity would generate enough counts to produce a good image with higher velocity. The first experiment was performed with the injection needle under the field of view. A syringe with 3 mL of F-18 that has activity of 30 mCi is injected over 60 seconds. The actual flow test has an average Reynolds number of about 1300. The experimental results from the first PET test are compared to corresponding CFD results and the Dye test results. The second test has the same exact experimental setup as the first PET test. One exception is that the injection needle is positioned outside of the field of view, which results in less radiation contribution to the detectors from the needle and fitting which may produce a better image. The main concern with placing the needle outside of the field of view is the test section orientation. In this case, 4 plastic beads are dipped into the F-18 solution and placed on the top test section inside the field of view. The 4 beads are arranged in an L shape to indicate the test section position and direction of the flow. The injection is also done with 3 mL of 22 mCi of F-18, but injection time is 30 seconds in the second case.

### 4.3 2x2 Validation Cases: CFD and Dye test

A CFD simulation is constructed in the COMSOL multiphysics, and its results compared with the data from the first PET test. The CFD simulation uses a k- $\epsilon$  turbulence model to predict the advective diffusion in the 2x2 test section. All input parameters are obtained from the first PET test. The COMSOL model is shown in figure 4.6.

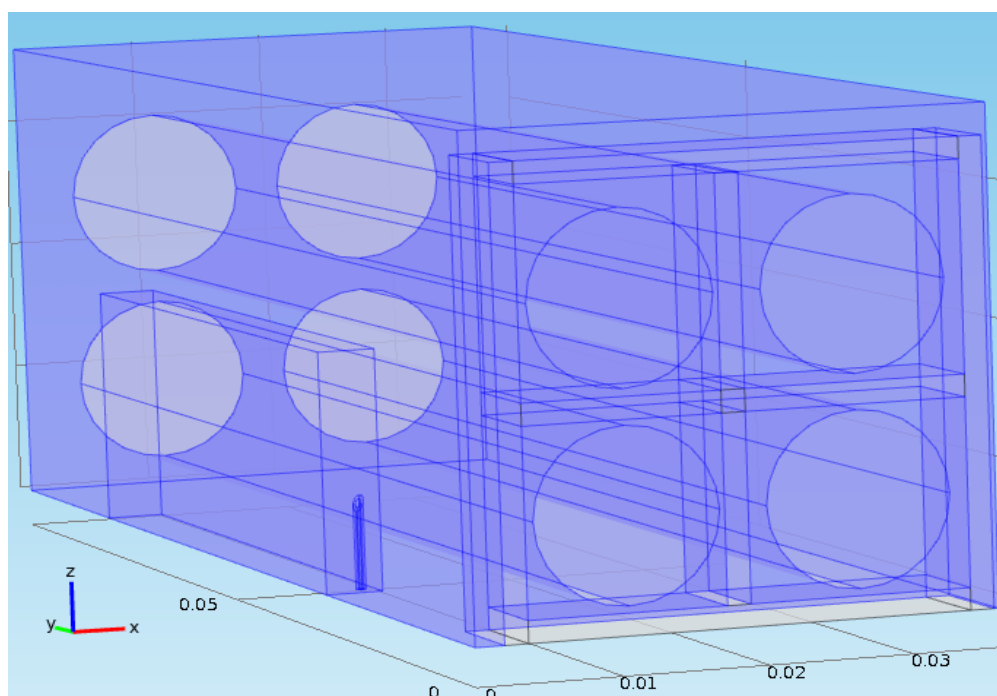


*Figure 4.6: Model in the COMSOL*

The COMSOL multiphysics platform does not have the capability to simulate radioactivity. A temperature variation between the injected and bulk fluids was used as an analogy to monitor the diffusion process. The temperature difference is 40 degrees Celsius between the bulk flow and injection flow. Two layers of computational meshes are used to compute this model. The meshes are shown in figure 4.7.



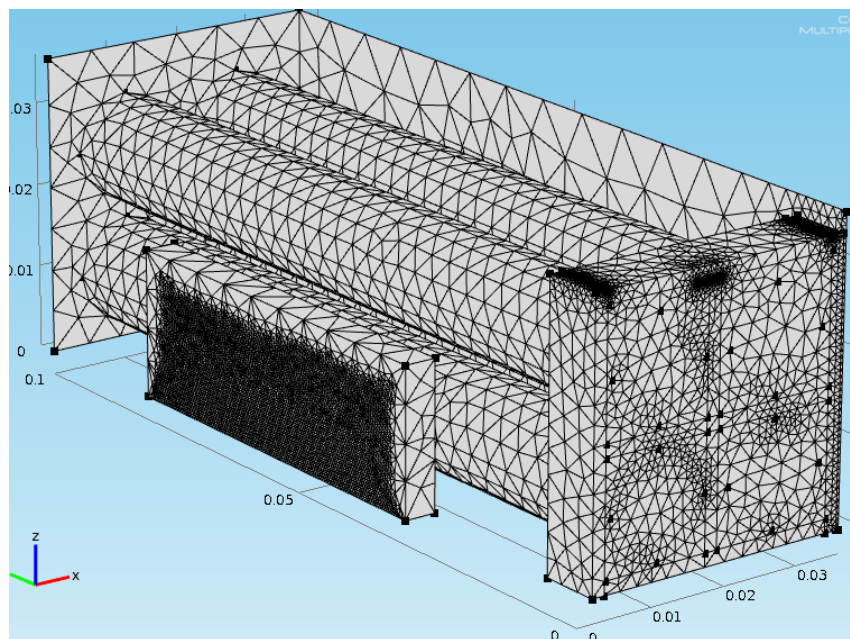


*Figure 4.7: Computational Meshes*

A super condensed mesh with a maximum size of 0.0005 m and a minimum element size of  $2e-6$  m is constructed in the region where mixing is more probable.

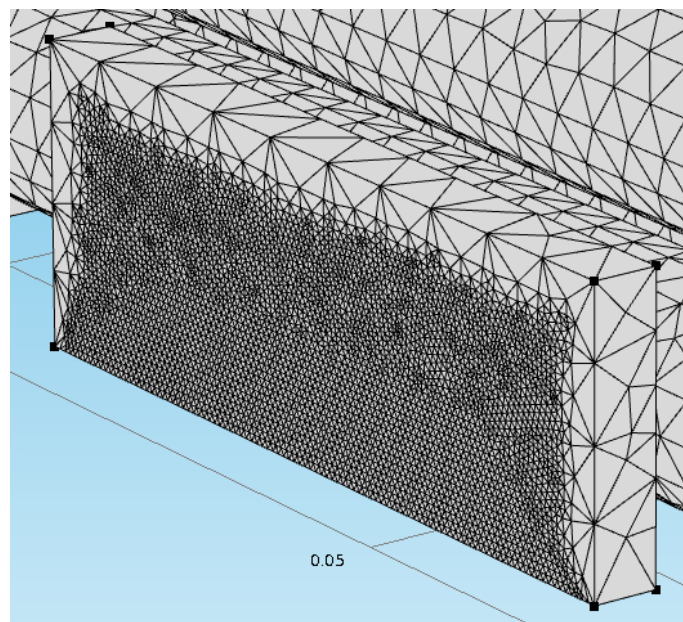


*Figure 4.8: Super Fine Mesh*

A relatively coarse mesh is used for rest of model. This CFD model has a total of five-hundred thousand meshes and 3.5 million degrees of freedom. The computational process is intensive; it took about 10 hours of continuous processing to compute using a workstation with a dual quad processor and 64 GB of RAM.

A dye test was performed using food coloring in the 2 x 2 acrylic test sections. The experimental setup and parameters are also the same as the first PET test. The diffusion process of the dye in the flow is captured using a high speed camera. The results of the dye test are used to compare with the CFD result and the PET result.

#### **4.4 Aluminum Rod Test Section**

The next test subject is aimed to be a more realistic engineering test section that has material properties of an electrical heater rod commonly used to simulate nuclear fuel. An electrical heater rod is made up of zircoloy, boron carbide, Nichrom V, magnesium boron nitrite and nickel. The transmission rate for coincident photons is estimated for a single heater rod to be approximately 68%. The detailed information and the attenuation calculation for a heater rod can be found in appendix B. A solid aluminum rod appears to be a good representation material for the heater rod composite attenuation. A single 0.5 inch aluminum rod has an equivalent attenuation rate to that of a heater rod, which is approximately 26%. In addition, aluminum is inexpensive and can be easily machined. The test section used in test case 3 is a square array of 3 by 3 aluminum rods in a test section with side equal 6.35 cm. The aluminum rod arrangement is shown figure 4.9.



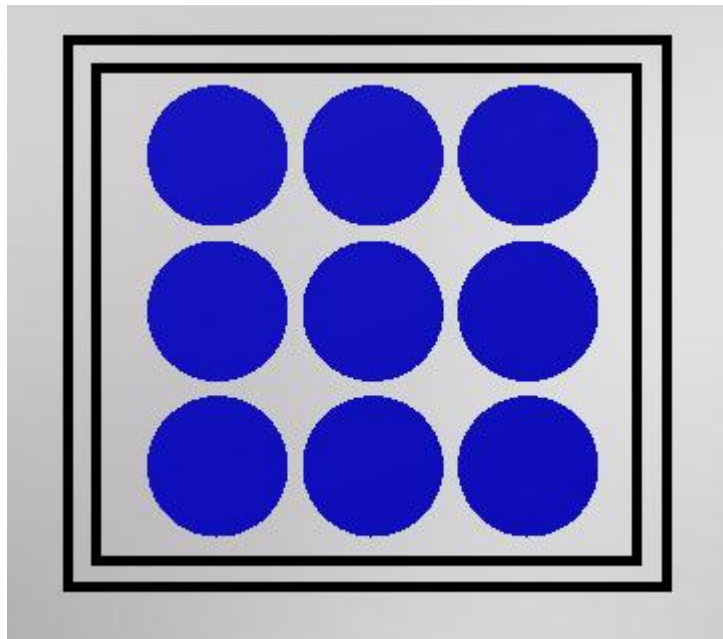


*Figure 4.9: 3 X 3 Square Array*

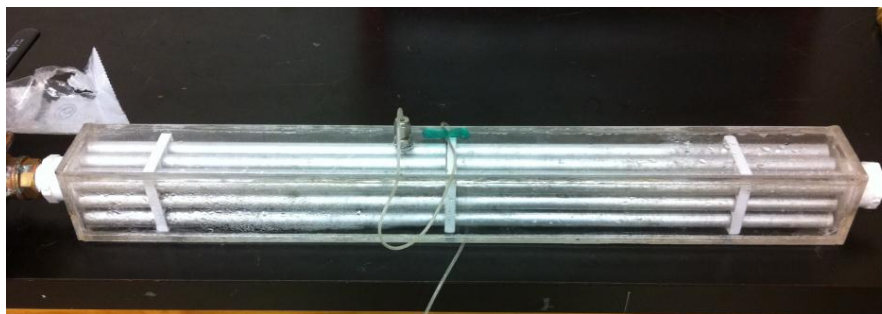


*Figure 4.10: The Aluminum Rod Test Section*

The injection needle is in red color and is positioned between the first and second columns of aluminum rods, as shown in figure 4.11.

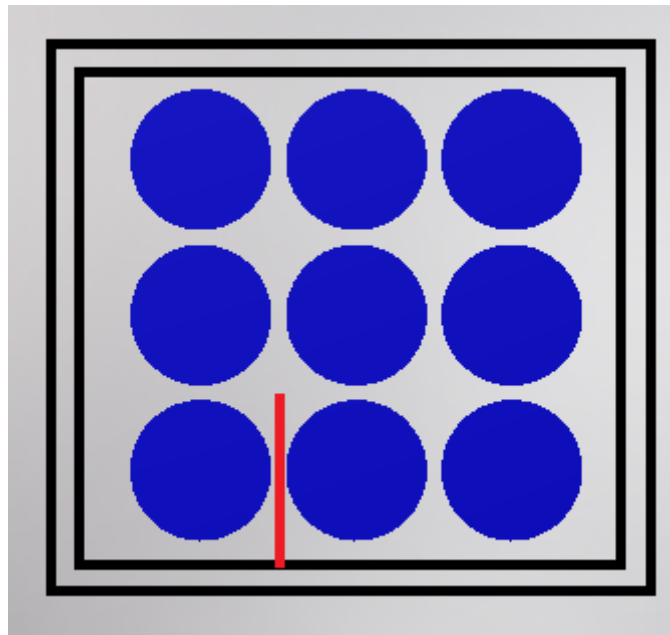


*Figure 4.11: Needle Location*

The flow rate is designed to be much higher than the previous two tests; the Reynolds number is approximately 3800. A 5 mL volume syringe containing 3 mL of F-18 with activity of 50 mCi is injected over 30 seconds.

## Chapter 5

### Results and Discussion

PET results shown in this chapter are reconstructed with the iterative reconstruction algorithm called MAP. PET results can be visualized with Asipro, Amira and Inveon Research Workspace (IRW). These software are capable of visualizing PET data in 2D and 3D. Asipro can analyze both static and dynamic formats of PET data. Amira is a post-processing software that is mainly used for static images. IRW is one of the most expensive and comprehensive visualization software for PET image visualization available. It is capable of visualization and analysis of static and dynamic PET images in 2D and 3D. Different visualization software have variability in the display of the PET image. Most of the results present in this section are analyzed with the IRW and the Amira.

The 3D static image of the first PET result in fluid studies is visualized in Amira, as shown in the figure below.

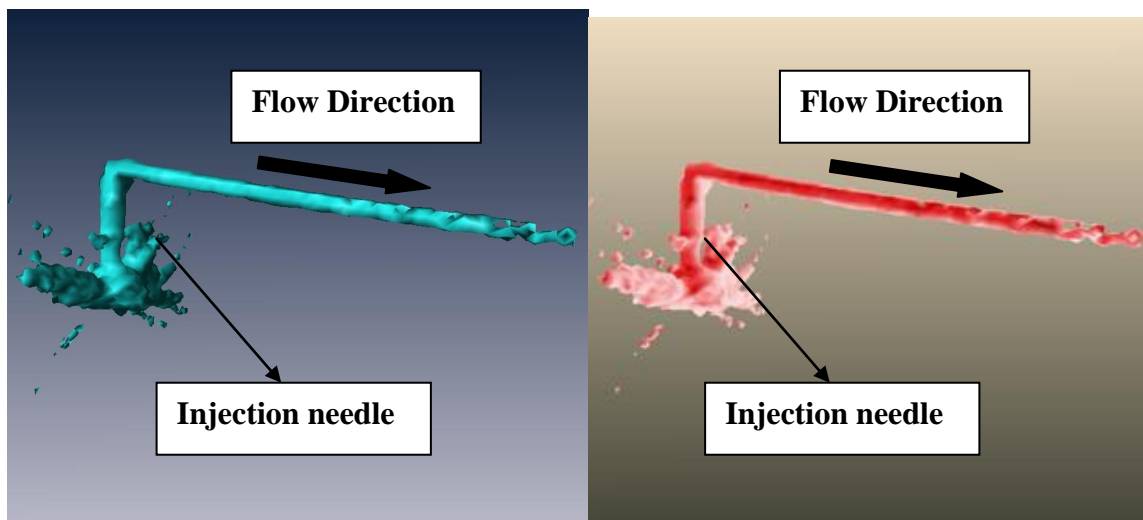


*Figure 5.1: 3-D Surface Contour of First Experiment Result from Amira*

This is a 3-D surface contour of the static image including the needle and plume. The plume's shape is expected for a diffusion process in laminar flow. The injection needle slightly fattens as a possible effect of radiation scattering along with the very high activity intensity in the needle in conjunction with the 1.8 mm FWHM scanner resolution. There are some artifacts on the bottom left of the picture that are more prominent, which are due to the scattering from the stainless steel fitting used for the needle penetration. The needle fattening effect is more obvious in a 2-D center slice of the plume, as shown in figure 5.2.

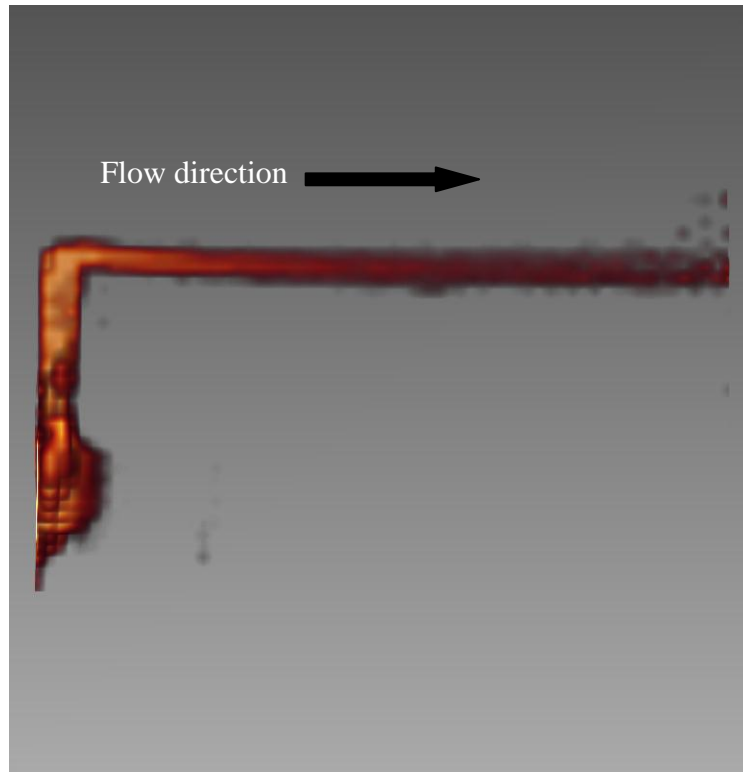


*Figure 5.2: PET Result in AsiPro*

The above static image is taken from AsiPro. An image enhancement is defined as a process of manipulating an image to improve its suitability for a specific application. In Amria, the PET image has different color scheme options, such as rainbow, and using the power log function for the image activity per unit volume spectrum better shows activity distribution in the plume. The results of an enhanced median plane slice PET image are shown in figure 5.3. Mathematic image processing algorithms can improve image appearance, but also introduce uncertainty to the measured activity value. It is expected that the injection needle is the most radioactive region, which is shown as red color. Lighter colors denotes lower levels of radioactivity, which is occur in the region further away from the needle.

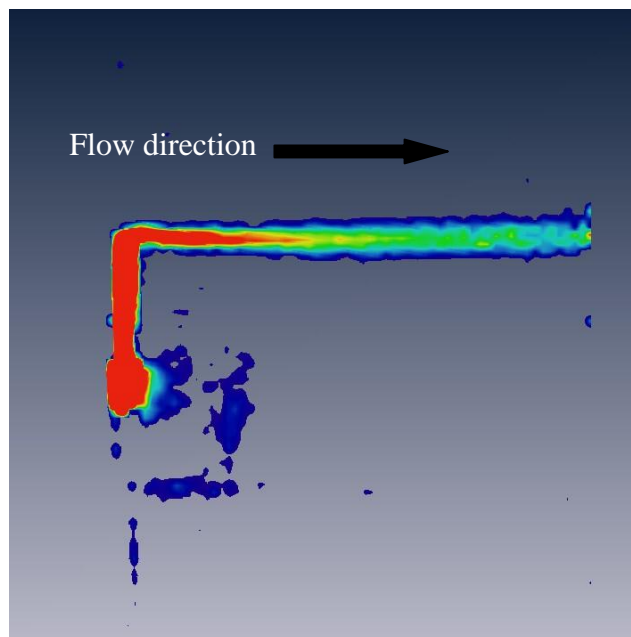


*Figure 5.3: Enhanced PET result in Amira*

The original slice static PET image result does not have the image enhancement algorithm applied. This is used to compare with the dye test result as shown in figure 5.4. Since the dye test results are captured with a high speed canon camera, a single picture only contains a portion of the static data. The static image for the dye result shown in figure 5.4 is made up of multiple pictures of the dye test from the same experiment.

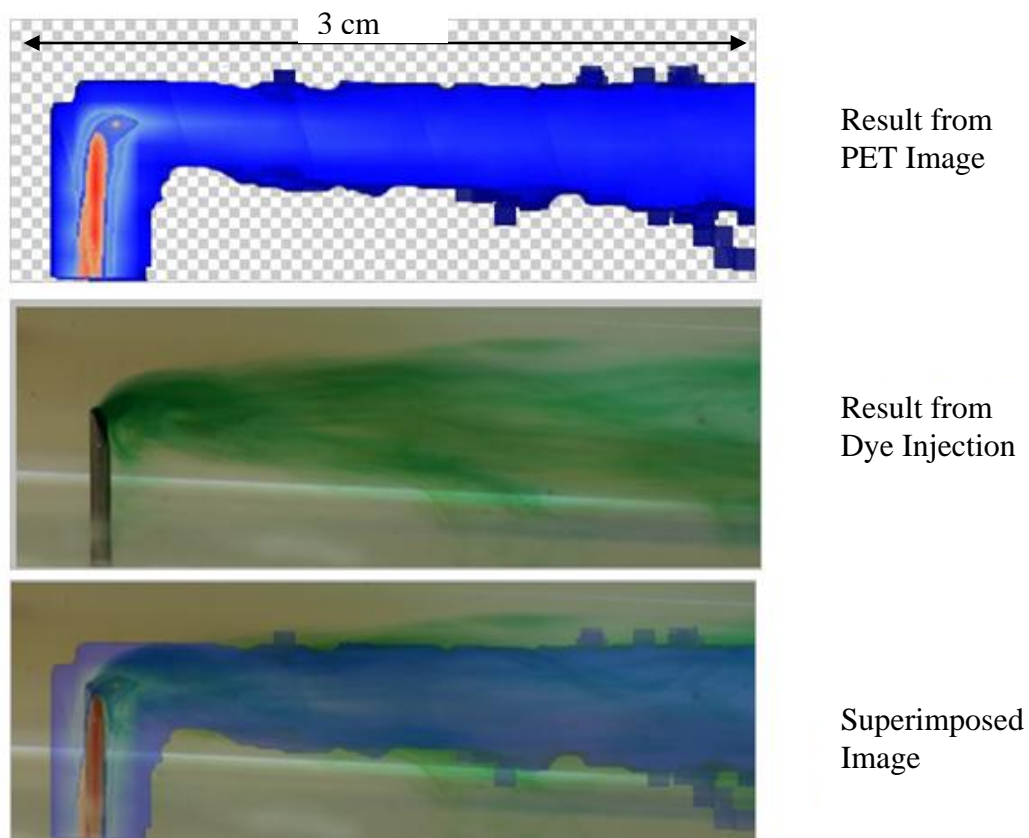


*Figure 5.4: Result Comparison for PET and the Dye Test*

The PET result and the dye test result have close qualitative agreement. The needle fattening effect is more pronounced in the superimposed image. A comparison between the dye test result and the COMSOL simulation result is made and shown in figure 5.5.

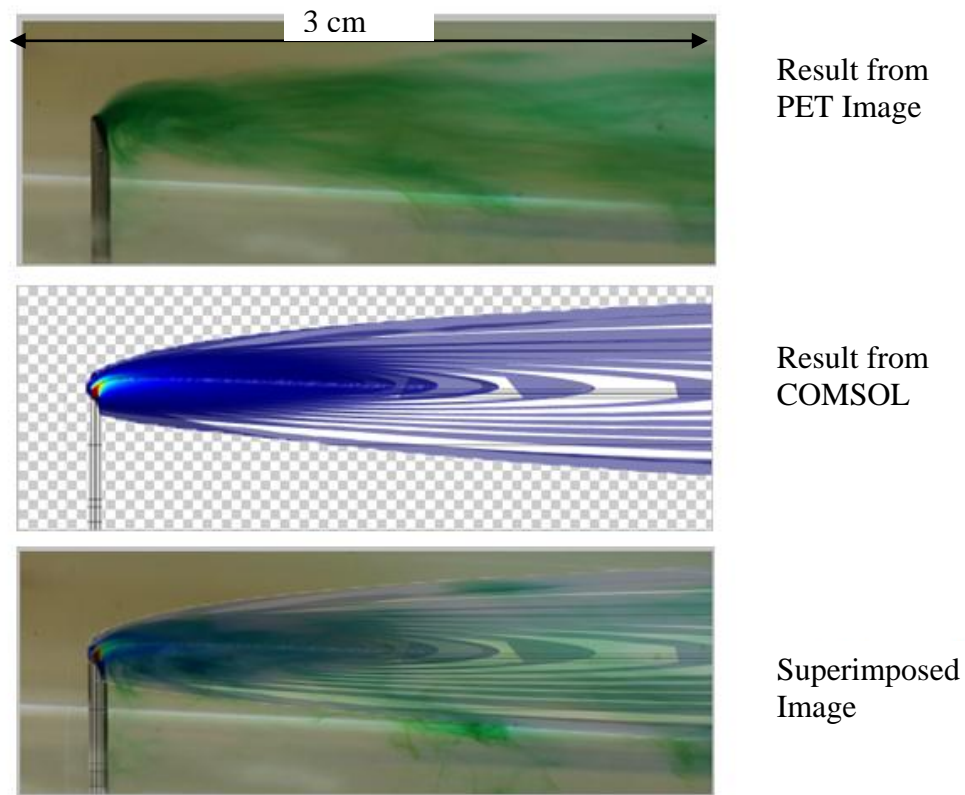


*Figure 5.5: Results Comparison for the COMSOL Model and the Dye Test*

The dye test result matches the COMSOL result reasonably well. The PET and COMSOL static results are compared in the sagittal or median plane and in the axial direction as a function of distances downstream of injection. Comparison in the sagittal plane and the axial plane are 2D, which is then used to reassemble a 3D assessment. The direct 3D comparison between a PET result and a COMSOL result is not available due to the lack of a 3D evaluation environment. The sagittal plane comparison is shown in the figure 5.6.



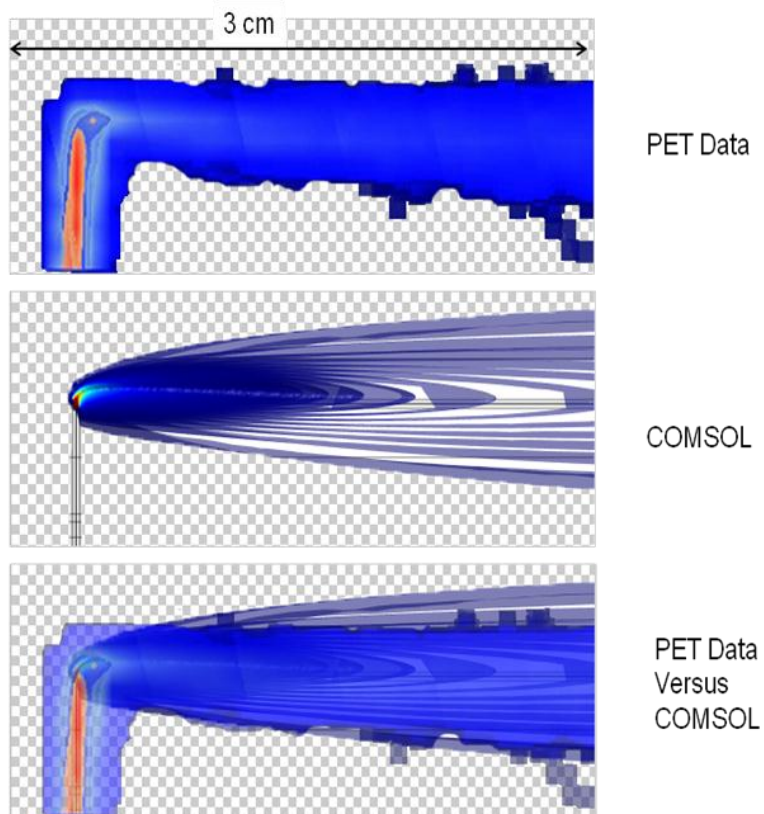


*Figure 5.6: The Median Plane Comparison for Results from the PET and the COMSOL*

The PET and COMSOL data are sliced in the axial direction at 2 cm, 4 cm and 6 cm downstream of the injection needle, as shown in figures 5.7 and 5.8 respectively. The injection needle is visible in figure 5.7, due to the use of a ghosting option that faintly includes upstream activity distributions.

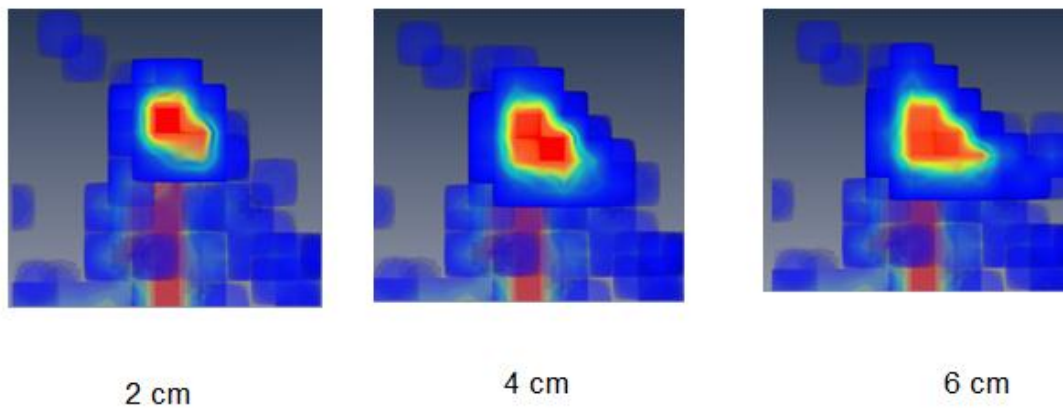


*Figure 5.7: Axial Slices for the PET Result at Specific Locations*

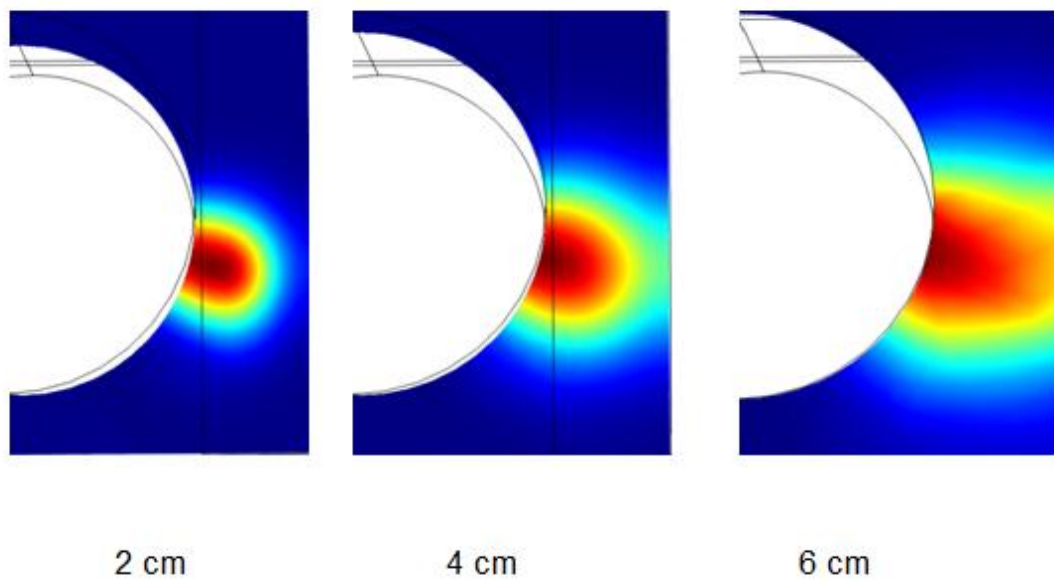


*Figure 5.8: Axial Slices for the COMSOL Result at Specific Locations*

Figure 5.9 indicates the physical characteristics of the predicted plume and PET measured plume are similar.

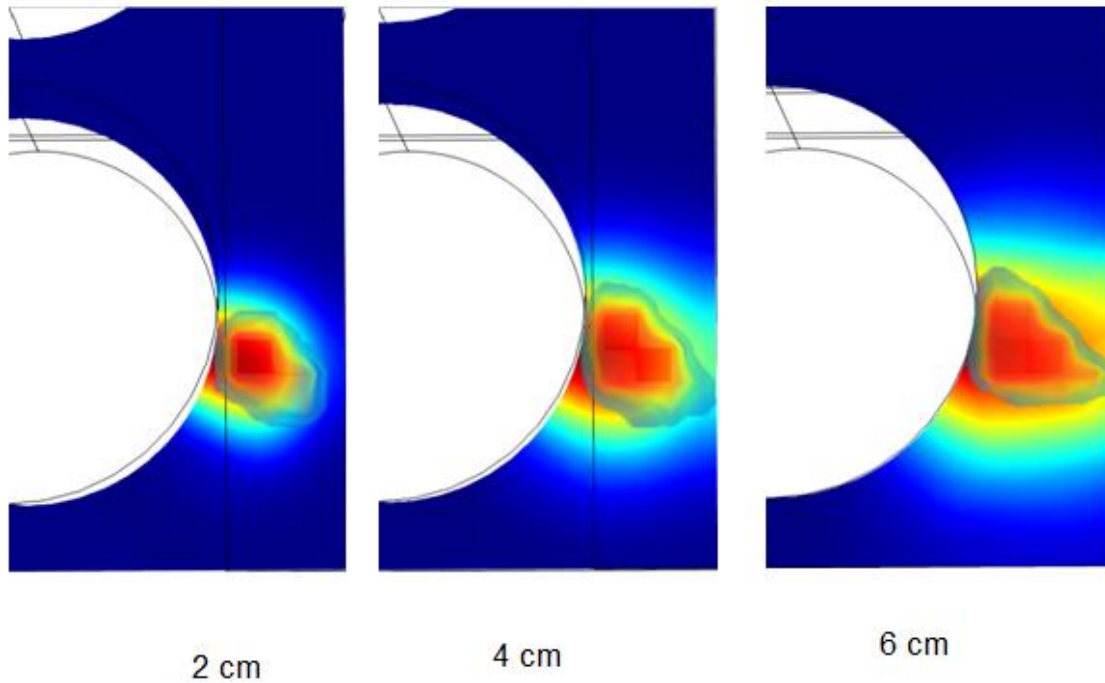


*Figure 5.9: Axial Slices of the COMSOL and the PET Result Comparison*

This case study shows PET is a useful tool for simple fluid studies that can be used to validate CFD simulation. PET data are also available in dynamic format, but a direct comparison between dynamic data on CFD and PET is currently not possible. A 3-D dynamic comparison environment will first have to be coded and constructed. The static PET results are also analyzed in IRW. It is interesting how the display quality is improved while using this software. IRW view of PET result is shown in the figure 5.10. The legend for activity distribution is available in IRW, and the activity distribution and the color map relationship are more clearly defined. It is hard to see the legend label in the figure 5.10, a closer look is shown in figure 5.11.

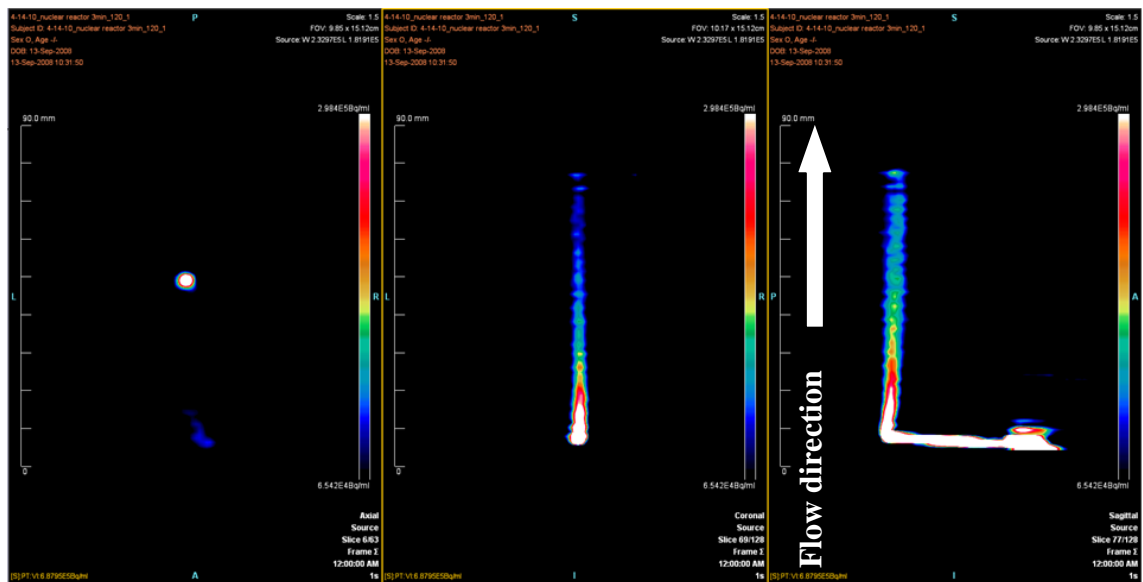
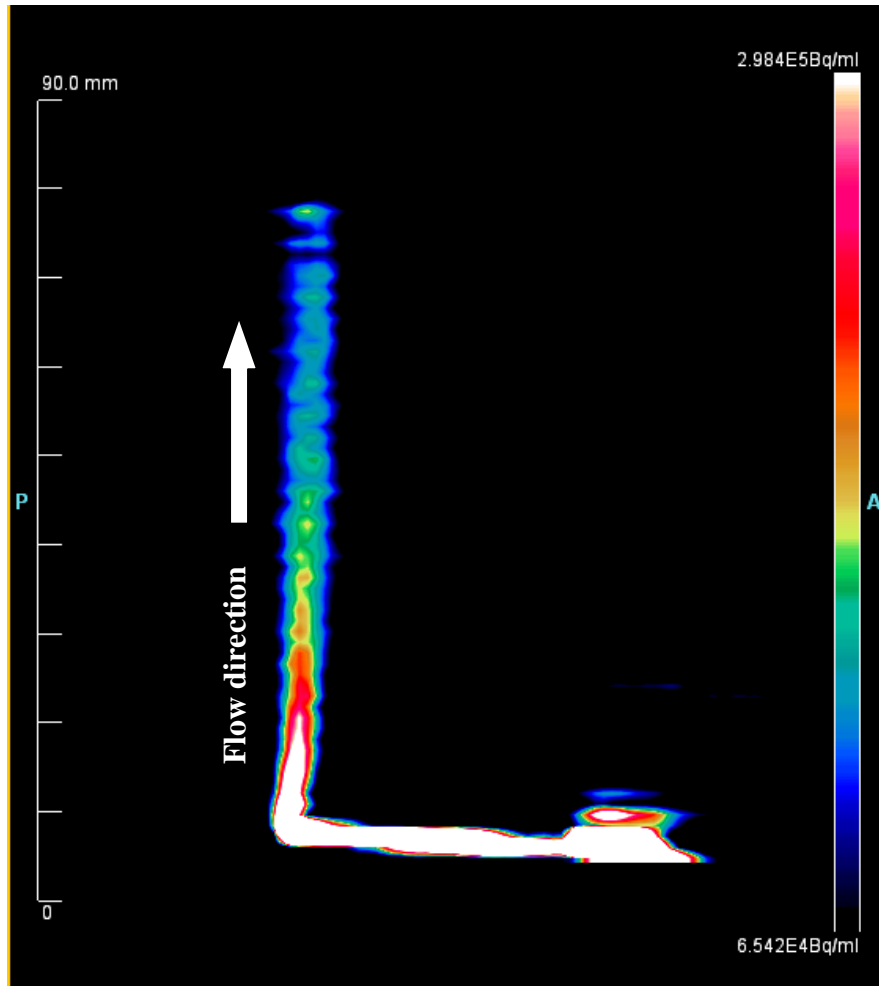


Figure 5.10: Different View of 1<sup>st</sup> Test Result in IRW



*Figure 5.11: A Closer View of the Result in IRW*

In figure 5.11, the plume appears to be fluctuating and discontinuous in some sections.

The size of the plume also can be measured using a built-in rule function. An axial slice has a thickness of 1.2 mm. The plume volume measured as a function of the axial slice number is shown in figure 5.12.

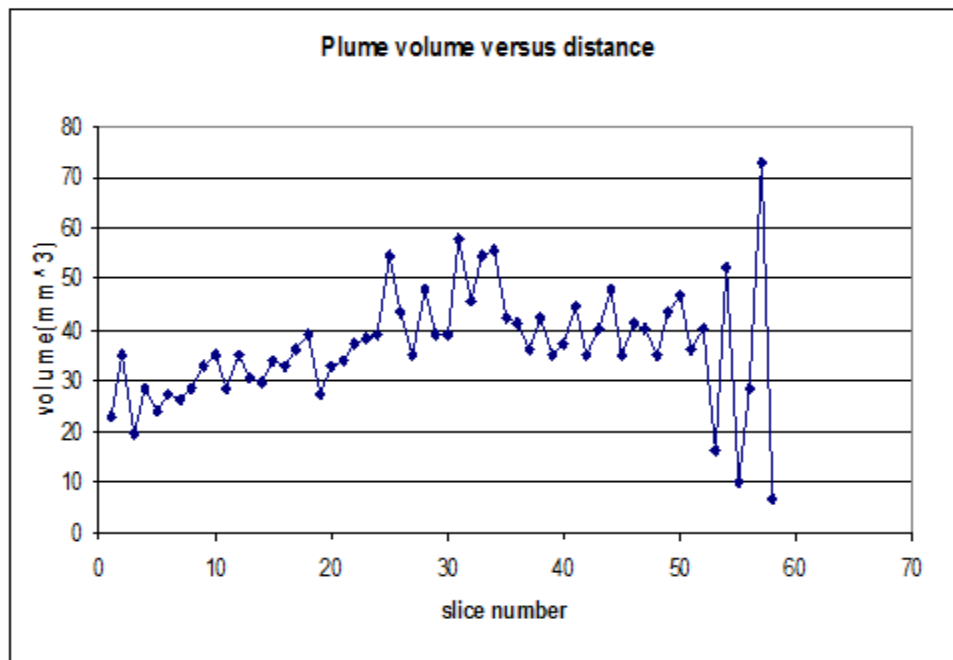


Figure 5.12: Plume Volume versus Distance

In the PET dynamic data, the activity is plotted as a function of time and is shown in figure 5.13.

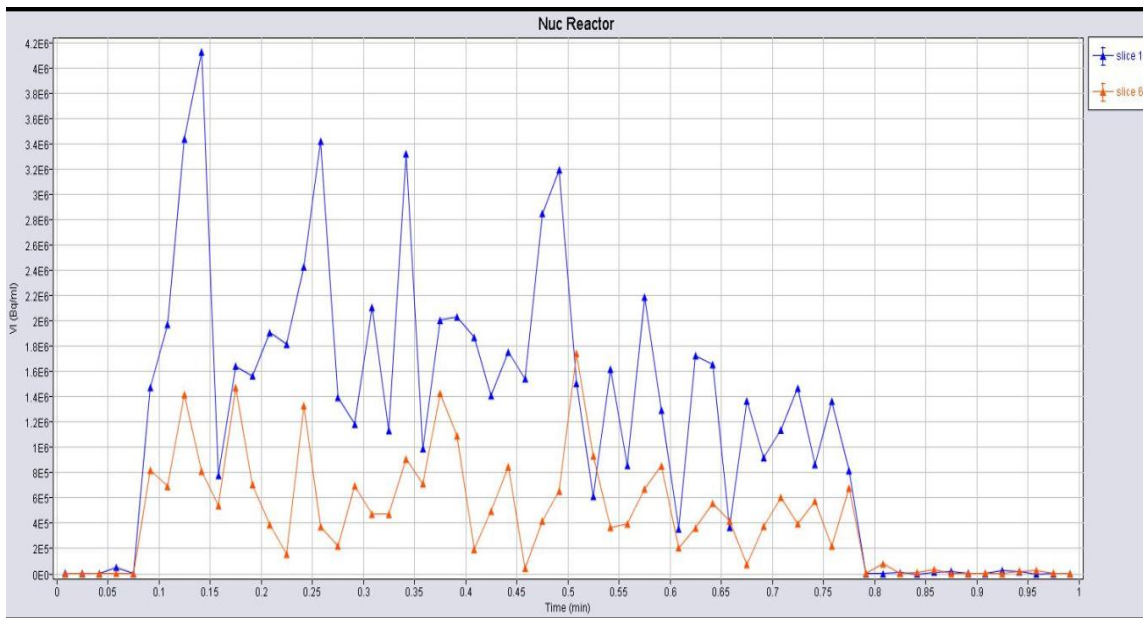


Figure 5.13: The Activity as Function of Time

Total time registered is about 45 seconds. The activity fluctuations are unexpected, and indicate possible inconsistent activity injection from the syringe pump. The activity per unit volume as a function of distance is plotted and shown in the figure 5.14.

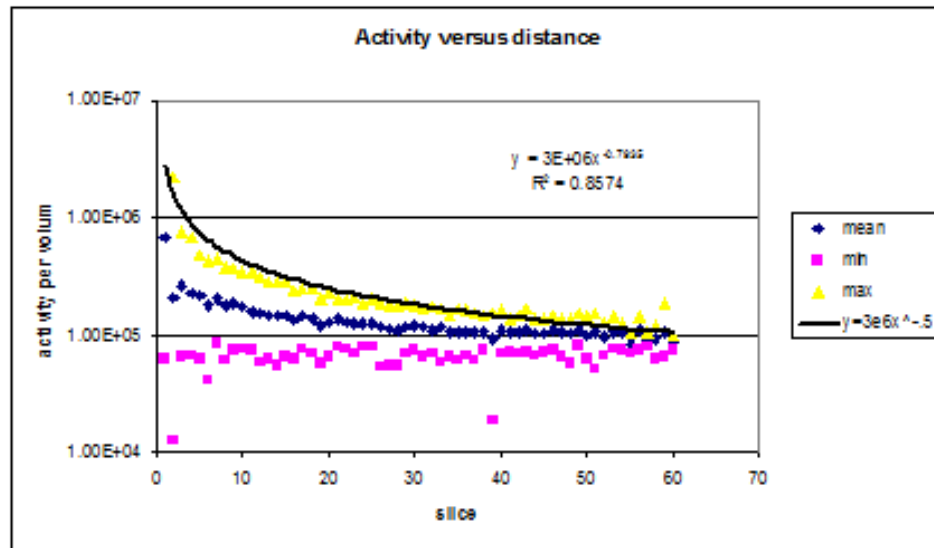


Figure 5.14: Activity as Function of Distance

The total test time average activity as a function of distance behaved as expected and confirms the activity distribution displayed in IRW.

As for case 2, the needle was placed outside of the field of view to obtain a better image of activity distribution within the plume. The result is shown in figure 5.15.

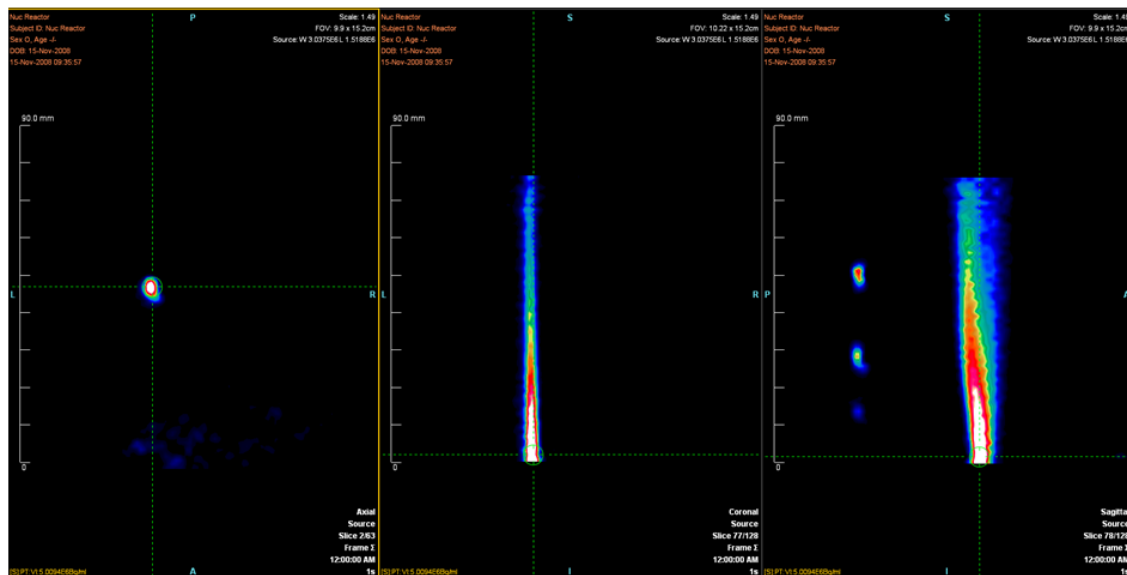


Figure 5.15: 2nd Experiment Result

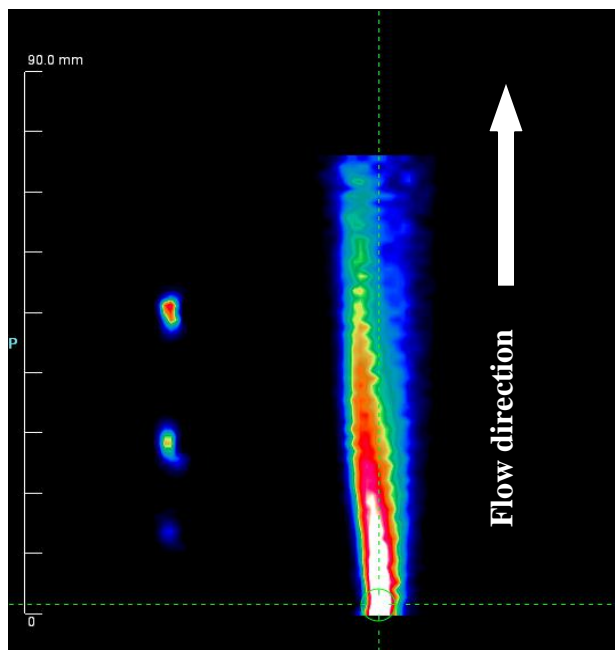
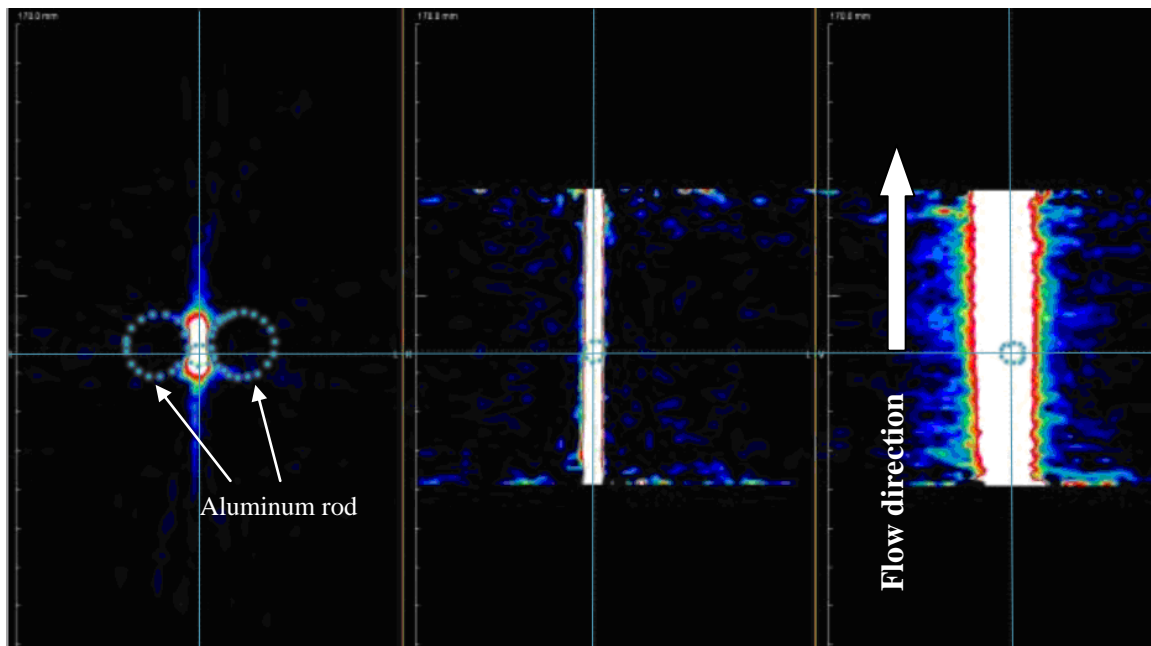


Figure 5.16: Slice View of the Plume



The direction indication beads are visible in figure 5.16. The activity distribution is improved significantly in comparison to placing the needle under the field of view. A slight fluctuation within the plume can be seen.

The results of the experiment in the 3X3 aluminum rod test section with Reynolds number 3800 is shown in figure 5.17.



*Figure 5.17: Different Views of Experiment 3 Result*

The image for this test section which contains a higher Z material shows the effect of scatter. No attempt to correct for scatter is included here. The injection rate for this third test is much faster than in the previous two tests due the different size of syringe that was used. This was unexpected and upset the test protocol. The syringe was a 5 ml syringe, which is approximately two times bigger in cross section than the 3 ml syringe used in the previous experiments. The shape of the image indicates that the radioactive tracer diffusing between the aluminum rods as shown in the leftmost view of figure 5.17. This

third test was completed just two months prior to this thesis defense and the data evaluation and comparison to computational outcomes remains for future work.

## Chapter 6

### Conclusion and Future Work

Studies of flow advective diffusion in a fuel rod bundle are performed using PET, dye injection and CFD. In the first experiment, PET data show the expected diffusion pattern and compare well with companion dye injection and CFD outcomes. A stainless steel fitting produced scattering artifacts that are visible in the PET data. The second PET test results shows significant improvement in contrast when the injection needle is excluded from the scanner's field of view. A reasonable image was obtained in the third test using nine 1.27 cm diameter aluminum rods in the test section. However, the scattering effects are much more apparent in the third test when compared to the PET data from the second PET experiment where acrylic rods are used.

The result comparison for the first PET test, a CFD simulation in COMSOL and the dye injection test showed that PET is a useful tool for flow studies. The dye test results validated the COMSOL results in a 2D comparison. Comparison of PET and COMSOL outcomes showed qualitative agreements in the measured and predicted flow diffusion. Additional efforts in PET data handling are required before more quantitative comparisons are possible.

High Z material, such as stainless steel adds scattering artifacts to PET images. The needle fattening effect and scattering artifacts around the stainless steel fitting in first PET case are caused by the increased scatter probability associated with high Z material. The presence of high Z materials increased the activity uncertainty and reduced image

resolution. Hot spots, such as the injection needle under the field of view, also posed a challenge for PET scanner. Gammas from the needle contributed too many image counts and saturated detectors in the ring. This reduced counts available to create the image of the diffusing plume.

Scattering effects could be reduced with a current PET and CT combined modality scanner. CT generates an attenuation map for test sections that contain higher Z materials. Attenuation maps can be used for scatter correction that will improve overall performance of PET for flow measurement. Commercially available PET scanners have much faster count rates; they are approximately 100 times faster than MicroPET P4 used for these tests, and they are available with companion CT scanners. Advanced scanners would make PET imaging in faster flows possible with tracer activities comparable to those used in these studies.

These experiments have shown that PET is a promising tool for fluid flow studies to validate CFD simulation. PET is fundamentally different from traditional fluid measurement tools such as PIV and LDV. PET makes studies in opaque systems and opaque fluids possible. The 511 KeV coincidence photons can penetrate a reasonable thickness of the metal boundary, for example 1 cm of steel, to enable studies in completely enclosed test sections.

### List of References

1. Anger, H.O., "scintillation camera." Review Science Instrument, Vol. 29 :27-33, 1958.
2. Briks, J.B., The Theory and Practice of Scintillation Counting. London: PergamonPress, 1967.
3. Arthur Ruggles, "Some Ideas For Metrology to Extend Capability and Attract Investors and Users from Methods Development Communities." The University of Tennessee Nuclear Engineering.
4. Blumgart, H. L., Weiss, S., "Studies on the velocity of blood flow." Journal of Clinical Investment, Vol 4:15-31, 1927.
5. Cherry, Simon R., Sorenson, James A., Phelps, Micheal E. Physics in Nuclear Medicine. 3<sup>rd</sup> ed., Philadelphia: Sauders, 2003.
6. De, Heversy G., "Radioelements as tracers in physics and chemistry." Chemistry News, Vol. 108:166, 1913.
7. De, Hevesy G., "The absorption and translocation of lead by plant: A contribution to the application of the method of radioactive indicators in the investigation of the change of substance in plants." Biochemistry Journal, Vol 17: 439-455, 1923.
8. Derenzo, Stephen E, "Mathematical Removal of Positron Range Blurring in High Resolution Tomography." IEEE Trans Nuclear Science, Vol. 33: 565-569, 1986.
9. Langer, Jens, "Development of a Parallel Computing Optimized Head Movement Correction Method in Positron Emission Tomography." University of Applied sciences Dresden and Research Center Dresden-Rossendorf, 2003.

10. Lawrence, E. O., Livingston, M. S., “ The production of high-speed light ions without the use of high voltage, *Physical Review*, Vol. 40: 19-30, 1932.
11. “MicroPET Facility” Waiseman Laboratory for Brain Imaging and Behavior, 2007. 15 June, 2011.
12. Mould, R.F, “A Century of X-Rays and Radioactivity in medicine.” Bristol, Institute of Physics, 1993.
13. Morgan, K. Z., Turner, J. E., “Principles of Radiation Protection.” Wiley, New York, 1967.
14. Myers, W.G., Wagner, H.N., “Nuclear Medicine: How it began.” *Hospital Practice*, Vol. 9: 103-113, 1974.
15. Nuclear Fuel Industries, Ltd. 2006, web. 14 June 2011.
16. Science in My Life. 2011, 15 June, 2011.  
<[http://scienceinmylife.com/?page\\_id=525](http://scienceinmylife.com/?page_id=525)>.
17. Schmidt, Frank W., Henderson, Robert E., Wolgemuth, Carl H. Introduction to Thermal Sciences: Thermodynamic, Fluid Dynamic and Heat transfer. New York: John Wiley & Sons, Inc., 1993.
18. Socologsky, Scott A., Jirka, Gerhard H., Environmental Fluid Mechanics Part I: Mass Transfer and Diffusion. 2<sup>nd</sup> ed. Germany, Karlsruhe: The University of Karlsruhe, 2002.
19. Tai, Yuan-Chuan, Ananya, Ruangma , et al. “Performance evaluation of the MicroPET Focus: A Third-Generation MicroPET Scanner Dedicated to Animal Imaging.” Oct 2004

20. Todreas, Neil E., Kazimi, Mujid S., Nuclear Systems I: Thermal Hydraulic Fundamentals. United States: Taylor & Francis, 1993.
21. Turner, James E., Atoms, Radiation, and Radiation Protection. Rev. 3<sup>rd</sup> ed., Weinheim: Wiley-VCH Verlag GmbH & Co., 2007.
22. Weber D, Eckerman KF, Dillman LT, et al. “Radionuclide Data and Decay Schemes.” New York, Society of Nuclear medicine, 1989.
23. Phelps, Michael E., PET: Physics, Instrumentation, and Scanners. New York: Springer, 2006
24. Parker, D. J., McNeil, P. A., “Positron emission tomography for process applications.” The University of Birmingham, UK. 1995.
25. Peters, S., Tschape, L., Zhang, B., A. Ruggles. “ V&V methodology comparisons: AIAA G-077(1998), ASME V&V 20 (2009), ASTM E1355-05a(2005), NEA/CSNI/R(2007), and NRC CSAU(1988).” NURETH 14 (2011).
26. Table of Nuclide. 7/19/2011. < [atom.kaeri.re.kr/](http://atom.kaeri.re.kr/)>.

## Appendix A

2x2

$$D_{et} = \frac{4D_e^2 - (N_p \pi D^2 - 8\sqrt{N_p} D_e t + 8 - 4N_p t^2 S)}{N_p \pi D + 4\sqrt{N_p} D_e S - 4N_p t S}$$

$$S = \frac{\text{total axial length of spacer}}{\text{Axial length of full bundle}}$$

$$= \frac{7.65 \text{ mm} \times 3}{2 \times 12 \times 254 \times 10} = 0.03765$$

$$D_e = 34.04 \text{ mm}$$

$$N_p = 4$$

$$t = 1.58 \text{ mm}$$

$$D = 12.7 \text{ mm}$$

$$D_{et} = \frac{4(34.04)^2 - (4\pi(12.7)^2 - 0.03765(8 \times 2 \times 34.04 \times 1.58) - 4(4)(1.58)^2 \times 0.03765)}{4\pi \times 12.7 + 4 \times 2 \times 34.04 \times 0.03765 - 4 \times 4 \times 1.58 \times 0.03765}$$

$$= \frac{2577.16}{168.89} = 15.26 \text{ mm}$$

$$Re = \frac{V D_H}{\nu}$$

$$\nu = 1.004 \times 10^{-6} \frac{\text{m}^2}{\text{s}} \text{ for water @ } 20^\circ\text{C}$$

For laminar for  $Re = 1500$ 

$$1500 = \frac{V (0.01526 \text{ m})}{1.004 \times 10^{-6} (\text{m}^2/\text{s})}$$

$$V = 0.09869 \text{ m/s}$$



3x3 Test Section

$$D_{\text{eff}} = \frac{4D_e^2 - (N_p \pi D^2 - 8 \sqrt{N_p} D_e t \delta - 4 N_p t^2 \delta)}{N_p \pi D + 4 \sqrt{N_p} D_e \delta - 4 N_p t \delta}$$

$$\delta = 0.03765 \quad \text{same as } 2 \times 2$$

$$D_e = 50.27 \text{ mm}$$

$$N_p = 9 \text{ Rods}$$

$$t = 1.58$$

$$D = 12.7 \text{ mm}$$

$$D_{\text{eff}} = \frac{4(50.27)^2 - (9\pi(12.7)^2) + 8 \cdot \sqrt{9} \cdot 50.27 \cdot 1.58 \cdot 0.03765 - 4 \cdot 9 \cdot (1.58)^2 \cdot 0.03765}{9\pi(12.7) + 4 \cdot 3 \cdot 50.27 \cdot 0.03765 - 4 \cdot 9 \cdot 1.58 \cdot 0.03765}$$

$$A_{\text{flow}} = 1369.88 \text{ mm}^2 \quad D_{\text{eff}} = 14.4 \text{ mm} = 0.0144 \text{ m}$$

$$Re \geq 4000 \text{ turbulent} \quad \nu = 1.004 \times 10^{-6} \text{ m}^2/\text{s}$$

$$Re = \frac{VDH}{\nu} \Rightarrow 4000 = \frac{V \times 0.0144}{1.004 \times 10^{-6} \text{ m}^2/\text{s}} = \frac{0.2789 \text{ m/s}}{1.004 \times 10^{-6} \text{ m}^2/\text{s}}$$

$$\text{Pipe Inner Diameter: } \frac{3}{4} \text{ in} = 1.905 \text{ cm} \Rightarrow \text{Radius} = 9.52 \text{ mm}$$

$$V_1 A_1 = V_2 A_2$$

$$0.2789(1369.88) = V_2 (\pi \times (9.52 \text{ mm})^2)$$

$$V_2 = 1.34 \text{ m/s}$$

$$i_{\text{in}} = 1.34 \times (\pi \times (0.00952)^2)$$

$$i_{\text{in}} = 0.382 \text{ L/s} \Rightarrow 22.92 \text{ L/min} = \frac{6.05 \text{ gallon}}{\text{min}}$$

3 x 3 test section

8.5 gpm discharge pump

$$\frac{8.5 \text{ gpm}}{1 \text{ g}} \left| \frac{3.785 \text{ L}}{1 \text{ L}} \right| \frac{1 \text{ Kg}}{1 \text{ L}} \left| \frac{1 \text{ m}^3}{1000 \text{ Kg}} \right| \frac{1 \text{ minute}}{60 \text{ s}} \left| \frac{5.362 \times 10^{-4} \text{ m}^3}{\text{s}} \right|$$

$$\dot{m} = v \cdot A \Rightarrow 5.362 \times 10^{-4} = v \cdot \pi \left( \frac{9.52 \text{ mm}}{1000} \right)^2$$

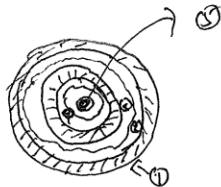
$$v = 1.88 \text{ m/s}$$

$$1.88 \cdot \pi (9.52)^2 = v \cdot (1369.88 \text{ mm}^2)$$

$$v = 0.3905$$

$$\boxed{Re = \frac{0.3905 \times 0.0144}{1.004 \times 10^{-6}} = 5600}$$

Appendix B



1. Zircaloy  $\approx 0.7$  mm thickness
2. Boron Carbide  $\approx 1.18$  mm thickness
3. Ni-chrome V  $\approx 0.7$  mm thickness
4. Magnesium boron nitride = 2 mm thickness
5. Nickel = 1.28

Zr  $\frac{w}{\rho} = 8.693 \times 10^{-2} \frac{\text{cm}^3}{\text{g}}$

$\rho = 6.4 \frac{\text{g}}{\text{cm}^3}$

B<sub>4</sub>C  $\frac{w}{\rho} = \sum w_i \left( \frac{w_i}{\rho_i} \right)$

$\rho = 2.52 \frac{\text{g}}{\text{cm}^3}$   $B = 8.72 \times 10^{-2}$   
 $C = 8.715 \times 10^{-2}$   $\left( \frac{w}{\rho} \right) \approx 8.72 \frac{\text{cm}^3}{\text{g}}$

ⓐ Ni-chrome: 80% Nickel 20% chrome by mass

Nickel:  $\frac{w}{\rho} = .08698$  chrome = .08281  $\frac{w}{\rho_{B\&C}} = 1.08615 \frac{\text{cm}^3}{\text{g}}$   $\rho = 8.4$

ⓑ Magnesium boron nitride (Mg<sub>3</sub>BN<sub>3</sub>)

54% Mg 8.6% Boron 33.3% nitride by mass  $\rho = 2$  Assumed.

Mg:  $\frac{w}{\rho} = .0864$  B:  $\frac{w}{\rho} = 8.72 \times 10^{-2}$  N = .0871

$\frac{w}{\rho}(\text{Mg}_3\text{BN}_3) = 1.08662 \frac{\text{cm}^3}{\text{g}}$   $\rho = 8.908$

ⓒ Nickel:  $\frac{w}{\rho} = .08698$

Transmission =  $\sum e^{-\mu_i x_i}$

=  $e^{-.08698 \times 8.908 \times 1.28}$   $\cdot e^{-.08615 \times 8.4 \times 0.7 \times 2}$   $\cdot e^{-8.72 \times 10^{-2} \times 1.14 \times 2}$   
 $\cdot e^{-.08693 \times 6.4 \times 0.7 \times 2}$   $\cdot e^{-.08615 \times 2 \times 2 \times 2}$

ⓐ

ⓑ

ⓒ

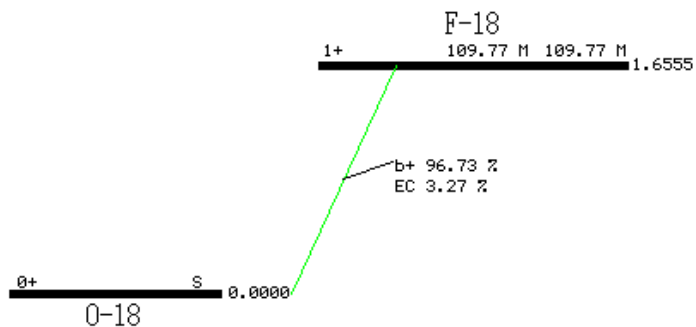
$\approx 67.8\%$  heater Rod.

74% for  $\frac{1}{2}$ " Al

## Appendix C

### 18F B+ DECAY

Parent state: G.S.  
 Half life: 109.77 M(5)  
 Q(gs): 1655.50(63) keV  
 Branch ratio: 1



Beta+ ray: total intensity =96.7

Max.E (keV)	Avg.E (keV)	Intensity(rel)	Spin
633.5 ( -)	249.8 ( 3)	96.73 ( 4)	1+
			0+

EC: total intensity = 3.3

Decay Scheme reference to Table of Nuclides [26]



## RADIONUCLIDE DATA SHEET Fluorine - 18



**F - 18**     9 protons     9 neutrons

**Radiation:**     Decay mode: Electron Capture

**Major Positrons:**

Max E (MeV)	Avg E (MeV)	# per 100 dis
0.633	0.250	97

Max. Positron Range in air     178 cm     or     5.67 ft  
Max. Positron Range in water     0.02 cm

**Major Gammas:**

E (MeV)	# per 100 dis
0.511	194

Avg. gamma E = 0.511 Mev

**Half-life:**     109.74 minutes     or     1.83 hours

**Gamma constant:**     7.72 mR/hr per 1 mCi at 30 cm

**Radiological data:**

Min. Ingestion ALI:     50000  $\mu$ Ci equals 5 rem TEDE (Whole Body)  
Min. Inhalation ALI:     70000  $\mu$ Ci equals 5 rem TEDE (Whole Body)

**Doses:**

Skin Dose:     Reported for 1  $\mu$ Ci over 10 cm<sup>2</sup> of skin  
                          177 mrad/hr (gamma dose)  
Point Source: 5,400 mrad/hr (positron dose)  
Disk Source:     5,400 mrad/hr (positron dose)

**Shielding data:**

Max. range for positrons:     Plastic     =     0.17 cm  
  Aluminum     =     0.1 cm  
Tenth Value Thickness for     Concrete     =     11.5 cm  
average gamma:     Lead     =     1.37 cm

**Detection Information:**     Usable Detectors listed with estimated efficiencies  
  (Use efficiencies listed on instrument when available)

Ludlum 3 with pancake probe at 1 cm:     9 %     Liq. Scint. Counter:     85 %  
Ludlum 3 with NaI probe near surface:     1 %     Gamma Counter:     25 %

**Action Quantities:**

Bench top quantity must be less than     500000  $\mu$ Ci  
Containers require labeling when greater than     1000  $\mu$ Ci  
Rooms require posting when there is greater than     10000  $\mu$ Ci  
Contamination lasting more than 24 hrs require NRC notification when greater than     250000  $\mu$ Ci

This F-18 Document is reference to the department of Environmental Health and Safety at the University of Missouri. 7/19/2011. <<http://ehs.missouri.edu/rad/isotopedata/f-18.pdf>>

### **Vita**

Bi Yao Zhang was born in FuZhou, China. He grew up in FuZhou and moved to Alcoa, Tennessee at the age of 13. He graduated from Alcoa High school on May, 2006. He continued his education in Nuclear Engineering at the University of Tennessee, Knoxville. He obtained his Bachelor degree of Science in nuclear engineering on May, 2010. He was working as an undergraduate research assistance during junior and senior year in college. He was supported as graduate research assistance from 2010 to 2011.